



HAL
open science

Polyhedral Voronoi diagrams for additive manufacturing

Jonàs Martínez, Samuel Hornus, Haichuan Song, Sylvain Lefebvre

► **To cite this version:**

Jonàs Martínez, Samuel Hornus, Haichuan Song, Sylvain Lefebvre. Polyhedral Voronoi diagrams for additive manufacturing. 2018. hal-01697103v1

HAL Id: hal-01697103

<https://inria.hal.science/hal-01697103v1>

Preprint submitted on 30 Jan 2018 (v1), last revised 14 May 2018 (v2)

HAL is a multi-disciplinary open access archive for the deposit and dissemination of scientific research documents, whether they are published or not. The documents may come from teaching and research institutions in France or abroad, or from public or private research centers.

L'archive ouverte pluridisciplinaire **HAL**, est destinée au dépôt et à la diffusion de documents scientifiques de niveau recherche, publiés ou non, émanant des établissements d'enseignement et de recherche français ou étrangers, des laboratoires publics ou privés.

Polyhedral Voronoi diagrams for additive manufacturing

Jonàs Martínez, Samuel Hornus, Haichuan Song, Sylvain Lefebvre
Inria

January 20, 2018

A critical advantage of additive manufacturing is its ability to fabricate complex small-scale structures. These microstructures can be understood as a *metamaterial*: they exist at a much smaller scale than the volume they fill, and are collectively responsible for an average elastic behavior different from that of the base printing material making the fabricated object lighter and/or flexible along specific directions. In addition, the average behavior can be graded spatially by progressively modifying the microstructure geometry.

The definition of a microstructure is a careful trade-off between the geometric requirements of manufacturing and the properties one seeks to obtain within a shape: in our case a wide range of elastic behaviors. As geometric requirements become stricter, it becomes increasingly difficult to design microstructures. This explains why most existing microstructures target stereolithography (SLA) and laser sintering (SLS) processes where requirements, while strict, are still more relaxed than that of continuous deposition systems such as fused filament fabrication (FFF).

In this work we introduce a novel type of microstructures that *strictly enforce* all the requirements of FFF-like processes: continuity, support and overhang angles. They offer a wide range of orthotropic elastic responses that can be freely graded spatially. This allows to fabricate parts usually reserved to the most advanced technologies on widely available inexpensive printers that also benefit from a continuously expanding range of materials.

1 Introduction

Novel capabilities of additive manufacturing processes are challenging the traditional separation between shape and material. Tool accessibility and mold extraction constraints no longer apply, and shapes with intricate internal details can be fabricated. These internal microstructures modify the large-scale material properties, making parts lighter, porous or flexible and resilient. In addition, these microstructures can be spatially graded: the same object may be rigid where external stresses apply, and lighter in other regions.

This has spawned an intense research effort towards the geometric design of microstructures that can be embedded into volumes while triggering varying properties. The microstructures are typically considered as a *metamaterial*: at large-scale they behave equivalently to a uniform material characterized by a homogeneous elasticity tensor. This average behavior can be analyzed, abstracting away the fine-scale details, in a process called *numerical homogenization*. In addition, the microstructures are often *parametric*: the geometry of their fine scale details is controlled through high-level parameters, such as thickness or orientation. These parameters impact the large-scale elastic behavior, and thus the observed elasticity tensor can be controlled by manipulating these parameters directly. The main interest in using such parametric metamaterials

is that their elasticity can be spatially controlled – graded – by a control field, varying mechanical properties within the shape volume. The control field can be either manually painted through a dedicated user interface [12] or automatically computed through, e.g. topology optimization [41].

In this paper we focus on defining a novel class of parametric metamaterials. A key challenge – besides triggering the desired elastic behavior – is to enforce constraints due to the additive manufacturing processes. Most existing works on the topic have focused on processes such as selective laser sintering (SLS) and stereolithography (SLA). These technologies have different constraints than the widely available and inexpensive fused filament fabrication (FFF) 3D printers. In particular, most recent works produce geometries exhibiting truss structures (detailed in Section 2). After slicing, these structures produce many isolated ellipses in each slice. These are extremely challenging to print on FFF systems, where continuity of deposition, low overhang angles, and support from below are strict requirements (for examples of actual trials we recommend the online article by Zhou [40]).

This is especially unfortunate, as FFF is not only widely available but allows to fabricate in a wide spectrum of materials, from inexpensive plastics, food-safe materials, nylons, to metal-polymer compounds and carbon fiber reinforced materials (see filament by *e.g.* *Proto-Plasta*). In addition, other technologies such as wire arc metal printing¹ and contour crafting² share the same constraints. These constraints are very restrictive and have so far prevented the development of metamaterials for these processes.

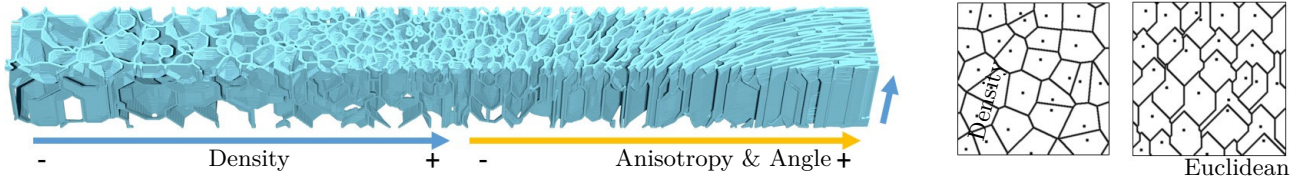
Contributions. Our paper aims at filling this gap, defining a novel parametric metamaterial with the following properties:

- closed-cell, stochastic foam-like geometry readily printable on FFF-like systems, with strictly enforced overhang angles and that is everywhere supported from below,
- density and anisotropy controllable through user provided fields that can vary arbitrarily,
- defines orthotropic materials that can be freely oriented in the plane orthogonal to the fabrication direction,
- a purely procedural computation that scales to arbitrarily large shapes.

This is made possible by defining procedural Voronoi diagrams based on polyhedral distances. We identify a class of parameterized polyhedral distances providing guarantees on the maximum overhang angles, and ensuring that all

¹See *e.g.* <https://waammat.com/about/waam>

²See https://en.wikipedia.org/wiki/Contour_crafting



Ours

Figure 1: *Left*: We propose a novel type of microstructures well suited for fabrication on continuous deposition processes such as fused filament fabrication. Our microstructures afford for a wide range of elastic behaviors, from isotropic to orthotropic. As illustrated their geometry can be spatially graded. *Right*: We model the foams as Voronoi diagrams of a special kind, which contrary to Euclidean Voronoi diagrams produce geometry enforcing all fabrication constraints.

deposited material is supported from below. These constraints remain enforced when varying density and orientation parameters. We detail the procedural generation of our foams, analyze their elastic behavior and the link between the underlying parameters and the obtained elasticity tensors, and produce a variety of results demonstrating applications.

2 Related work

Researchers in additive manufacturing have recognized the need for internal fill patterns early on [26]. Indeed, by avoiding densely filling an interior, the print time and material use are greatly reduced. Thus, early infill patterns were essentially targeted at reducing material density, while being fast to generate and efficient to fabricate. Typical patterns for continuous deposition encompass parallel lines with varying spacing, but more elaborate patterns have been devised in an effort to achieve better strength to weight ratios [19].

In the recent years, the focus has shifted to producing infill patterns with controllable mechanical properties. Most approaches cast the problem as a two-scale optimization [41]. A parametric metamaterial is defined either as a set of (parametric) periodic microstructures [34, 31, 30] or as a random process producing geometry [23, 24]. The link between the microstructure parameters and their average elastic behavior is analyzed, defining a material space. Each entry of the material space relates a choice of structure parameters to an elasticity tensor. Thus, a user or an algorithm can directly work at a coarser scale and specify the desired elastic behavior in different regions of space. This is then translated into microstructure parameters used to produce a final geometry. The definition of the geometry is often procedural, such that it is instantiated only when sent to the printer, slice by slice [32, 36]. Our work is inscribed in this direction of research.

Interestingly, most results in this area use SLS and SLA processes. This is largely explained by the fact that these technologies are less constrained than continuous deposition approaches, such as FFF. The challenges in designing infill patterns for continuous deposition are threefold. First, material can only be deposited on top of already solidified layers: it is not possible to start a new feature in ‘mid-air’. Similarly, while slanted walls can be fabricated, there is a limit to the maximum overhang angle (typically around 45 degrees, varies with layer and deposition thicknesses). Second, the extrusion process should be interrupted as little as possible, as each start/stop produces small deposition defects. Third, the deposition head is typically a relatively heavy device, and acceleration rates are limited by mechanical capabilities.

The first constraint (overhangs, support) relates to

the geometry of the patterns and requires defining *self-supporting* fill patterns (e.g. that do not require auxiliary support for fabrication). The two other constraints (continuity, acceleration) relate to deposition efficiency and quality. In particular, truss structures which print well on SLA/SLS are ill-suited for continuous deposition due to the last two constraints: they require printing many small discs spread throughout each layer. This triggers a large number of start/stop and abrupt speed changes – the low acceleration limiting the maximum reachable speed. As a consequence, the beams have lower quality and print slower than their volumes would indicate. Therefore, unsurprisingly, most patterns for FFF are comprised of as long as possible continuous lines.

Nevertheless, recent research has considered improved fill patterns for continuous deposition. Leary et al. [14] advocate for the use of self-supported spatial tessellations, considering maximum overhang angles. Wu et al. [38] explore how sub-dividable rhombic fill patterns [17] can be optimized for rigidity. Lee and Lee [15] optimize similar patterns to produce parts that are as empty as possible – while producing self-supported structures. Hornus et al. [8], Xie et al. [39] and Wang et al. [37] consider how to maximally carve parts while producing self-supported inner cavities. Lu et al. [20] optimize the positions of the point sites of a Voronoi diagram to strengthen an object. Interestingly, a soluble support material had to be used within the cells (page 6, paragraph *Physical test* of [20]) – that is because usual Voronoi diagrams cannot form self-supported structures (see Section 3). Lee et al. [16] pack many ellipses within a volume interior to obtain a self-supported interior fill.

However, none of these techniques afford for the definition of a material space, in the same sense as the microstructures employed with SLS/SLA [34, 31, 23]. One exception is the work of Martinez et al. [24] on orthotropic foams, where orthotropic 2D patterns are fabricated on FFF printers. However, this only applies to 2D patterns extruded vertically, not 3D structures. Subdivisible infills [27, 38] come close, but these cannot produce smooth spatial variations in orientation and density due to their underlying regular nature. We discuss them in more details and provide elements of comparison in Section 5.4.

Our work aims at introducing infill patterns which are well suited for fabrication by continuous deposition, can be graded spatially, and provide a wide material space for design.

3 Overview

The microstructures we explore belong to the family of closed-cell foams. They are defined as a stochastic process,

which parameters drive the small-scale material arrangement, and ultimately the average elastic behavior.

Our foams are defined as the thickening of the facets of Voronoi diagrams of a special kind. We give below some more specific background on the use of Voronoi diagrams to represent foams and microstructures, explain the challenges and give some intuition on our technique. The precise definition and analysis of our microstructures are given in Section 4.

3.1 Voronoi foams in additive manufacturing

In material science, naturally occurring cellular solids are often idealized as sets of Voronoi edges (open-cell) or facets (closed-cell) [6]. These have been well studied as they exhibit desirable properties such as an isotropic elastic behavior [21] with a quasi-linear link between density and Young’s modulus [6, 33].

Voronoi open-cell foams are used for fabrication on SLA/SLS processes, as they form fully connected truss networks well suited to resin and powder solidification. They are amenable to efficient procedural synthesis [23]. Open-cell foams are however not very suitable for continuous deposition, due to the constraints mentioned in Section 2. For continuous deposition, closed-cell foams are more promising: they form walls that would afford for continuous deposition and are also known to exhibit good mechanical behaviors – in fact, closed-cell foams are more rigid than open-cell foams (see [6, Formulas 5.6 and 5.13]). The reason closed-cell foams are not used with SLA/SLS is that they would trap non solidified material in closed cells. This, however, is not an issue on FFF-like processes.

Unfortunately, as we discuss next, the usual Voronoi diagrams do not define self-supporting closed-cell structures. Besides, their elastic behavior would remain limited to isotropic elasticity, while we seek a wider material space.

3.2 Challenges of usual Voronoi diagrams

We now discuss why usual (Euclidean) Voronoi diagrams cannot be readily used. Let us consider such a diagram defined from a uniformly randomly distributed set of point sites $s_i \in S$. Each Euclidean Voronoi cell is defined by:

$$V_P(s_i) = \{p \in \mathbb{R}^3 : \|s_i - p\|_2 < \|s_j - p\|_2, \forall s_i \neq s_j \in S\} \quad (1)$$

The closed-cell foam is formed by thickening the facets of the diagram. Figure 2 shows 2D examples where facets are edges. In these side views, the build direction goes upward. As can be seen in the Euclidean diagram (leftmost), the facets/edges can take an arbitrary orientation and many of them violate the overhang constraint: they cannot be printed on continuous deposition systems. In addition, when the point sites are uniformly distributed, the cells tend to be isotropic, which prevents the emergence of anisotropic elastic behaviors (see [24]).

3.2.1 Changing the distance

Voronoi diagrams can be defined using different distances. Figure 2 shows the diagram obtained using the L_1 and L_∞ distances on the same point sites.

While these diagrams are not printable – due to the horizontal facets – an interesting emerging property is that the facets take only a fixed number of different angles. This, in fact, is a property of any Voronoi diagram under a *polyhedral distance*: a distance induced by a convex polyhedron [22, 9].

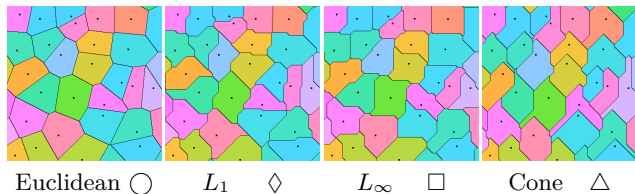


Figure 2: The Voronoi diagram of a set of points under various distances, with their unit ball drawn next to the name.

Our intuition is that some specific convex polyhedron must exist that induces polyhedral Voronoi diagrams whose facet set is fully fabricable. Figure 2 (rightmost) shows an initial test that confirmed this intuition: using a cone distance produces a fully printable diagram. This idea forms the basis of our approach.

We detail how we build upon this initial intuition to define parameterized 3D Voronoi foams in Section 4. We analyze the mechanical behavior of the structures in Section 5 and demonstrate applications to additive manufacturing in Section 6.

4 Method

We now describe the use of polyhedral Voronoi diagrams for producing microstructures with spatially varying elasticity, well suited for continuous deposition (FFF-like processes).

Let $B_d = \{p : p_z = d\}$ be a plane orthogonal to the printing direction z , and $B_d^- = \{p : p_z < d\}$ be a half-space below B_d . We call *slope of a facet* or slope of a plane the dihedral angle between the plane supporting the facet and any horizontal (xy) plane. For example a vertical wall has slope $\pi/2$, the printing plane slope zero.

Our microstructure is defined by a mesh \mathcal{K} that must satisfy the following two fabrication constraints (see Figure 3):

1. **Angle constraint:** Each facet f of \mathcal{K} has to be “sufficiently close to vertical” so that it is printable with FFF. We model this constraint by imposing a lower-bound $\theta^* \in [0, \pi/2]$ on the slope of facet f . If n is the normal vector of facet f , it must satisfy $|n_z| \leq \cos \theta^*$. Reasonable values of θ^* may range, say, from $\pi/6$ to $\pi/3$ and depends on the fabrication hardware at hand.
2. **No-local-minimum constraint:** Each point $p \in \mathcal{K}$ has to be “supported from below” so that it does not appear mid-air during fabrication; i.e. we have that $\mathcal{K} \cap N(p) \cap B_{p_z}^- \neq \emptyset$ where $N(p)$ is any open neighborhood of p .

These two constraints are well-suited for FFF-like processes, as they capture the requirement that deposited material has to be well supported from below. For our purpose in this paper, we model the mesh \mathcal{K} as the union of the facets of a polyhedral Voronoi diagram, namely, the Voronoi diagram of a set of point sites that arises when using a specific polyhedral distance instead of the usual Euclidean one (Section 4.1.1). We show that some choices of distance polytopes guarantee that \mathcal{K} satisfies both fabrication constraints. In particular, we show how one can easily check that a given polyhedral distance entails a fabricable mesh \mathcal{K} (Section 4.1.3) and we exhibit a simple family of such polytopes (cones, Section 4.2). We discuss which parameters can be spatially graded and how (Section 4.3). Finally, in Section 4.4 we detail a simple algorithm to extract the deposition paths delineating to the Voronoi facets.

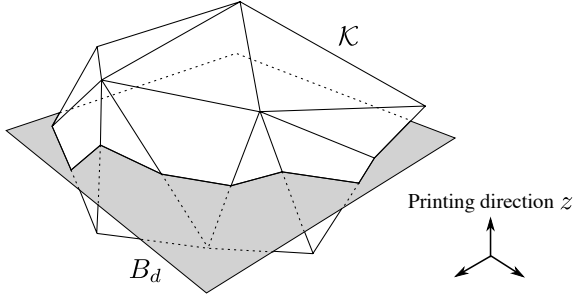


Figure 3: Illustration of fabrication constraints. The plane B_d is shown in gray. The slope of all facets of \mathcal{K} is greater than 45° . The no-local-minimum constraint is satisfied everywhere in \mathcal{K} .

4.1 Polyhedral Voronoi diagrams

We now recall the definition of polyhedral distances and their use in Voronoi diagrams. For simplicity, some of the following illustrations consider a planar polygonal distance.

4.1.1 Polyhedral distances

Let $P \subset \mathbb{R}^3$ be a compact convex polyhedron of combinatorial size k containing the origin in its interior. The *polyhedral distance* induced by P from a point p to q is (e.g., [29]):

$$d_P(p, q) = \min \{t \geq 0 : q \in p + tP\}. \quad (2)$$

The value of $d_P(p, q)$ is the minimal scaling factor t applied to P so that $p + tP$ touches q (Figure 4). Note that the L_1 and L_∞ distances are particular cases of polyhedral distances. Since P is convex, the triangle inequality holds: $0 \leq d_P(p, r) \leq d_P(p, q) + d_P(q, r)$. However, d_P is symmetric if and only if P is centrally symmetric with respect to the origin.

The distance $d_P(p, q)$ can be computed as follows [10]. Let q' be the unique point of $p + P$ intersected by the ray from p to q (see Figure 4). Then $d_P(p, q) = \frac{\|q-p\|}{\|q'-p\|}$.

In our implementation, we compute the closest intersection of the ray with the planes supporting the facets of P .

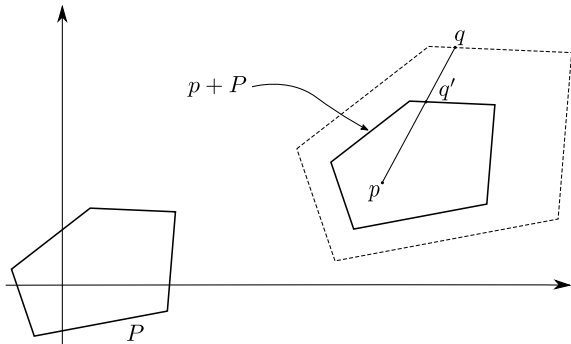


Figure 4: A polygonal distance function.

4.1.2 Polyhedral Voronoi diagrams

Equipped with the polyhedral distance, we now describe their use in Voronoi diagrams. Let S be a set of n point sites in \mathbb{R}^3 . The *polyhedral Voronoi diagram* $\text{Vor}_P(S)$ is the

decomposition of \mathbb{R}^3 into Voronoi cells. A cell $V_P(s_i)$ for a site $s_i \in S$ is defined as:

$$V_P(s_i) = \{p \in \mathbb{R}^3 : d_P(s_i, p) \prec d_P(s_j, p), \forall s_i \neq s_j \in S\} \quad (3)$$

where the lexicographical distance relation \prec is necessary to deal with cases where a full region space belongs to the bisector (non-general position cases [13]), see Figure 5:

$$d_P(s_i, p) \prec d_P(s_j, p) \iff d_P(s_i, p) < d_P(s_j, p) \vee (d_P(s_i, p) = d_P(s_j, p) \wedge (i < j)) \quad (4)$$

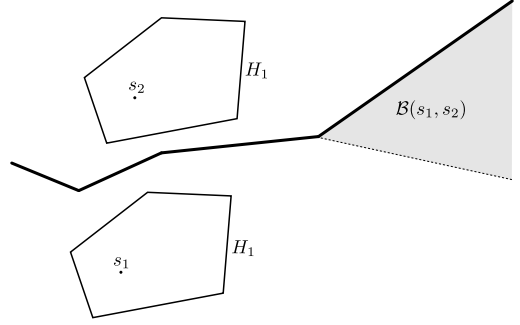


Figure 5: A non-general position case: the line passing through s_1, s_2 is parallel to the line containing the facet H_1 of P . The gray region are points of the polyhedral bisector $\mathcal{B}(s_1, s_2)$. The lexicographical distance of Equation (4) selects one of the boundaries of the gray region.

The Voronoi facets form the boundary set of Voronoi cells. Due to the triangle inequality, the Voronoi cells are star-shaped polyhedrons [4]: for all $q \in V_P(s)$ the line segment from s to q is in $V_P(s)$. Regarding the combinatorial complexity, assuming the complexity k of P is *constant*, the worst case complexity of the Voronoi diagram is $\Theta(n^2)$ [9] ($n = |S|$).

The bisector between two point sites p and q is the set of points equidistant to p and q under the distance d_P . An important property for our purpose is that the facets of $\text{Vor}_P(S)$ form a *subset* of the arrangement of the bisectors of each pair of sites in $S \times S$ (see, e.g., [22]). Thus, if all the bisectors satisfy both fabricability constraints then the facets of the Voronoi diagram form a fabricable mesh as well. We now analyse polyhedral bisectors in more detail.

4.1.3 Polyhedral bisectors

In this section, we recall known facts about polyhedral bisectors and explain how these properties can be used to check whether the geometry of P induces *fabricable* bisectors.

The polyhedral bisector between two point sites p and q is:

$$\mathcal{B}(p, q) = \{r \in \mathbb{R}^3 : d_P(p, r) = d_P(q, r)\} \quad (5)$$

Note that the polyhedral distance is taken *from* p and q to r because d_P is not symmetric. Various works have already studied this kind of polyhedral bisectors [5, 11, 25]. For a more detailed exposition, we refer the reader to the thesis of Ma [22] and the references therein.

For simplicity, we assume that p and q are in general position with respect to P . That is, the line through p and q is not parallel to any line segment contained in the boundary of P [1]. Then, $\mathcal{B}(p, q)$ is piecewise linear and homeomorphic to a plane [22]. We give a method to construct the bisector of two point sites in the supplemental material.

We say that two features (vertex, edge or facet) $X \subset P$ and $Y \subset P$ on the boundary of the distance polytope P generate a feature B of the bisector $\mathcal{B}(p, q)$ when $B = \{(p + \lambda X) \cap (q + \lambda Y) \mid \lambda > 0\}$. B is either empty or does not depend on the relative position of the point sites p and q . It follows from the constructions of polyhedral bisector (detailed in the supplemental material) and Proposition 1 below, that each linear feature of a bisector is generated by two features on P .

To determine fabricability, we have to analyse the slope of these linear features. This builds upon the following property. Let B_{ij} be a facet of the bisector $\mathcal{B}(p, q)$ generated by the facets f_i and f_j of P . Let n_i be the outward normal vector to facet f_i . Let $\alpha_i > 0$ be the distance from the origin to the plane H_i supporting f_i . (In particular, if r is a point of f_i then $\alpha_i = r \cdot n_i$.)

Proposition 1. Write H_{ij} for the plane that spans the origin and the line $H_i \cap H_j$. Then, the bisector facet B_{ij} (generated by f_i and f_j) is parallel to the plane H_{ij} (Figure 6). The normal vector of B_{ij} is proportional to $\alpha_j n_i - \alpha_i n_j$.

The proof is in [9]. The derivation of the formula for the normal vector can be found in the supplemental material. Given Proposition 1, we now explain how to check if both fabrication constraints are respected.

Verifying the angle constraint Each planar facet B_{ij} of the bisector $\mathcal{B}(p, q)$ is defined through the interaction between two facets f_i and f_j of P (see Figure 6). Proposition 1 tells us that the normal vector of B_{ij} depends only on f_i and f_j and is independent of the relative position of p and q . Thus, there are at most $\binom{k}{2}$ different orientations for the bisector facets. We can check that they satisfy the angle constraint by enumerating all pairs of facets of P .

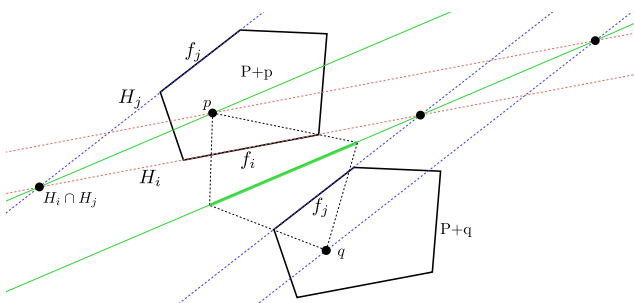


Figure 6: Let f_i, f_j be facet of P . Let H_i and H_j be the supporting planes of f_i and f_j , respectively. The feature of $\mathcal{B}(p, q)$ generated by f_i and f_j is drawn bold and green. A construction for its supporting plane is shown. Lines with the same color are parallels. The bold green bisector feature is indeed parallel to the top green line, as constructed in Proposition 1. See Lemma 3.2.1.2 in [22].

Verifying the no-local-minimum constraint Similarly, the vertices of all bisectors exhibit only a finite number of configurations that we can also enumerate in time $O(k^2)$, to verify that no vertex of any bisector is a local minimum with respect to the build direction. Each bisector vertex is generated by either an edge-edge pair or a vertex-facet pair (see Figure 7). Details are given in the supplemental material.

In summary, for a given polyhedral distance d_P induced by a polytope P of size k , we can check if the polyhedral bisectors under d_P satisfy both fabrication constraints.

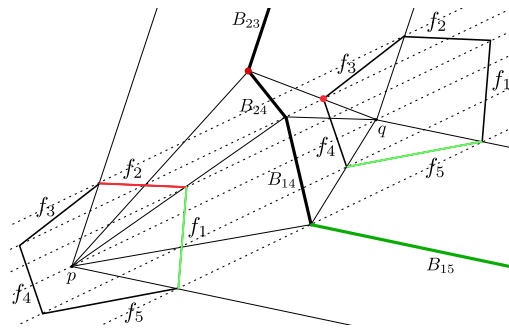


Figure 7: Polyhedral bisector between two point sites p and q . Each facet B_{ij} of the bisector is generated by facets f_i on $p + P$ and f_j on $q + P$. The dark-red bisector vertex is generated by the two light-red features of P . The dark-green bisector edge is generated by the two light-green features of P . A section in the supplemental material details this geometric construction.

4.2 Polyhedral cone distances

We now describe our choice of a particular family of polyhedral distances that induce fabricable Voronoi diagrams. The ideal family has few parameters and the influence of each parameter should be well understood, and easy to relate to the final elastic behavior. We prefer a distance that is symmetric around the z -axis so that it is easier to reason about. The most difficult property to achieve is the absence of local minimum.

We determined that a polyhedral cone achieves these objectives, and we now describe our family of cone distances. Given the parameterized cone geometry (Section 4.2.1), we explain how the fabrication constraints are satisfied (Section 4.2.2) and extend the family with anisotropic cones (Section 4.2.3). We highlight the influence of the parameters on the induced Voronoi diagram in Section 4.3.

Size: k	Slopes: θ, μ		Anisotropy: σ, ζ	
$3 \leq k$	$\theta^* \leq \theta < \pi/2$	$0 < \mu < 1$	$0 < \sigma < 1$	$\zeta \in \mathbb{R}$

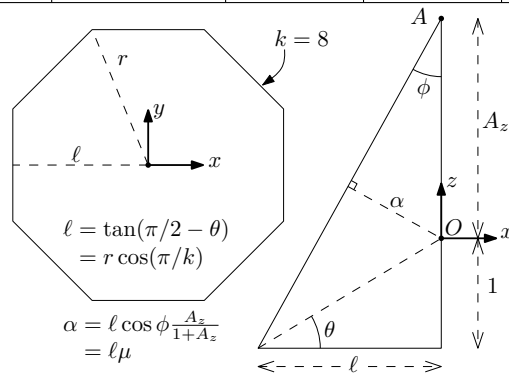


Figure 8: *Top.* The parameters describing our family of distances. *Bottom.* The geometry of the cone for $k = 8$. The right triangle is the half of the cone cutaway in the plane (O, x, z) . We indicate remarkable quantities used in computations.

4.2.1 Geometry of the cone

The *base facet* of the cone is a horizontal regular k -gon (Figure 8-bottom-left). The cone has k *side facets* (typically $k = 8$). The scale of the distance polytope does not affect the Voronoi diagram that it induces, so we assume that

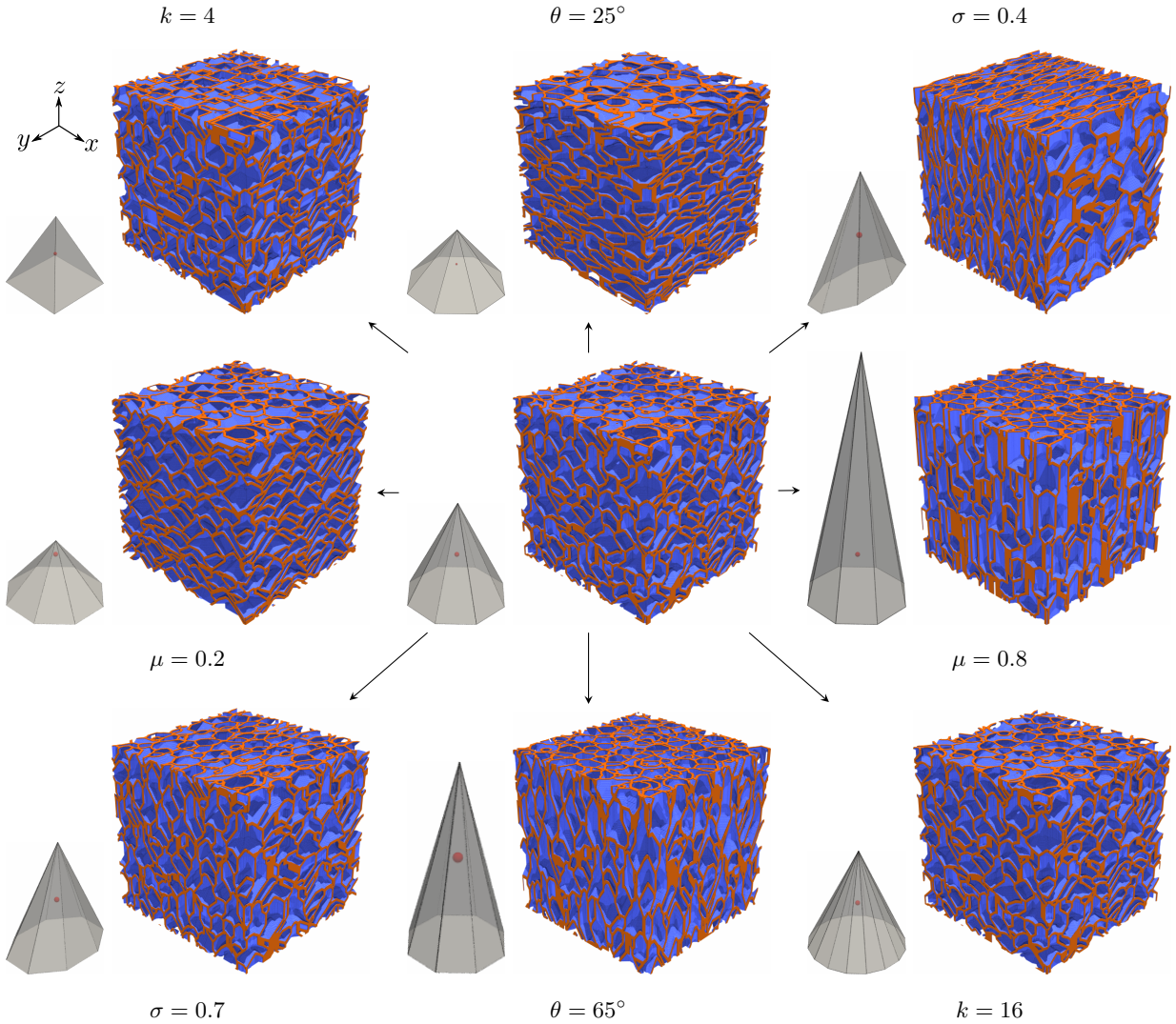


Figure 9: Illustration of cone parameters and effect in the corresponding polyhedral Voronoi diagram. For better understanding, the boundary of the cube is highlighted in orange color. The central sample has parameters $k = 8$, $\theta = 45^\circ$, $\sigma = 1.0$, and $\mu = 0.5$. Each neighbouring sample vary a single parameter. We provide in the supplementary material illustrations for a wider variation of parameters.

the base facet lies at $z = -1$. The cone has apex $A = (0, 0, A_z)$ with $A_z > 0$. (Figure 8-right). The vertices of the base facet have $y, -x$ -coordinates: $r \cos a_i$ and $r \sin a_i$ where $a_i = (2i + 1) \frac{\pi}{k}$ for $i = 0..k - 1$, and r is the radius.

We parameterize the cone with parameters k, θ, μ and σ , ζ for the anisometric case (Figure 8-top). All other quantities are determined from these parameters to enforce fabrication constraints (Section 4.2.2). Examples of cones within our family are shown in Figure 9.

4.2.2 Cones for fabricable Voronoi diagrams

We now consider constraints on the slopes of the bisector features to determine the geometry of the cone from its parameters.

All the side facets contain the apex A of the cone, thus if H_i and H_j are planes supporting two side facets f_i and f_j , their intersection line contains A as well. By Proposition 1, H_{ij} contains both A and the origin O , so that it is a vertical plane. We conclude that any bisector feature generated by two side facets is vertical and therefore satisfies the angle constraint.

Let us now consider a feature generated by a side facet

and the base facet. By Proposition 1, this feature is parallel to a plane spanning an edge of the base facet and the origin. Its slope θ (Figure 8-bottom) is *the same* for all side facets. In order to satisfy the angle constraint, we choose the value of θ in the range $[\theta^*, \pi/2)$, where θ^* is the angle constraint bound. This fixes the value of $\ell = \tan(\pi/2 - \theta)$ and the radius $r = \ell / \cos(\pi/k)$ of the base facet.

The last value to determine is A_z . It comes from our parameter μ , which controls the distance α from the origin to a side facet. By expressing the sine of angle ϕ , we compute $\alpha = \ell \cos \phi \frac{A_z}{1 + A_z}$. In order to decouple parameters θ and μ , we interpret our parameter μ as $\mu = \alpha / \ell$. Then, by expressing the squared tangent of angle ϕ as $\frac{\alpha^2}{A_z^2 - \alpha^2} = \frac{\ell^2}{(1 + A_z)^2}$, we obtain $A_z = \frac{\mu}{1 - \mu^2} \left(\mu + \sqrt{1 + \ell^2(1 - \mu^2)} \right)$. Figure 10 shows a 2D example cone (a triangle). The table of possible bisector vertices shows the impossibility of a local minimum. We provide in the supplementary material an interactive applet illustrating the induced bisectors in 3D.

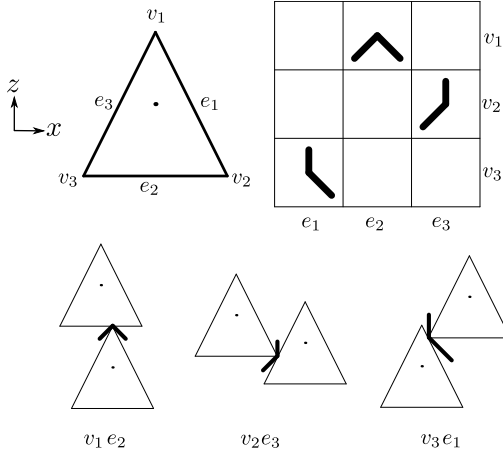


Figure 10: Polygonal distance defined by a triangle. The three different bisector vertex configurations are shown in the table, and in context below. The polygonal bisectors do not exhibit any local minimum, and form an angle of at least 45° with respect to the x axis.

4.2.3 Anisotropic cones

We vary the anisotropy of the polyhedral Voronoi diagram by shrinking the distance cone along the x axis prior to rotating it around the z axis. We do not allow other axes of rotation so as to guarantee that the Voronoi mesh stays fabricable: the base of the cone becomes a polygonal approximation of an ellipse and stays horizontal. The shrink is obtained by applying to the cone the linear transformation $\text{diag}(\sigma, 1, 1)$ where $0 < \sigma < 1$.³ The rotation angle is specified by an angle ζ . The analysis in Section 4.2.2 still applies. A pair of side facets generate a vertical bisector feature and the base facet generates features with slopes that vary for each side facet, but are always larger than or equal to θ . Figure 9 illustrates how the parameterization impacts the corresponding polyhedral Voronoi facets.

4.3 Spatial variations

The capacity to obtain gradients of properties within fabricated shapes is a major advantage offered by additive manufacturing. In this section we discuss how the geometric properties of our microstructures can vary spatially.

4.3.1 Varying the point sites density

The microstructures that we fabricate are materializations of the Voronoi mesh \mathcal{K} . We control their density by changing the set of point sites S on which the Voronoi diagram is computed, following an input density field $\mathbb{R}^3 \rightarrow \mathcal{D}$ where $\mathcal{D} \subset \mathbb{R}$ is a range of fabricable densities. In practice we follow the implementation of Martínez *et al.* [23] to produce point sites in a multi-resolution jittered grid.

4.3.2 Varying the polyhedral distance

We now consider that each of the parameters θ , μ , σ and ζ are fields in \mathbb{R}^3 . The value of the parameter is picked at the location of a point site $s \in S$, and used to define the distance polyhedron at s . Thus, we are effectively using a *different* distance for each site in S . We discuss two

³ Let η be the minimal slope of the bisector facets. In order to have η stay constant when we shrink the cone along the x axis, we generate the circle in the $y, -x$ frame so that the cone has at least one side facet perfectly parallel to the x axis.

subsets of parameters that can be spatially varied together while still guaranteeing fabricability in Section 4.3.3 and Section 4.3.4. We always consider $k \geq 3$ and $\theta \geq \theta^*$ constant.

Remark. When changing the distance at each site, the fact that the bisector between two sites p and q is homeomorphic to a plane does not hold anymore. In fact, in such a situation, the bisector can have more than one connected component [11]. We never observed this behavior in our experiments. This is due to the fact that point sites are distributed all over space so that pieces of bisectors that may appear far from their two parent sites are “taken over” by the Voronoi cells of other sites.

4.3.3 Varying μ

The apex of the cone moves vertically from just above the origin when $\mu \approx 0$ to infinitely high as μ approaches 1. Consider two side facets of two identical cones and start raising the apex of one cone (but not the other). Then, the feature that those facets generate becomes increasingly horizontal. The slope decreases but fortunately never reaches below θ .

While we do not have a formal proof, we can verify it numerically. Consider a side facet f_i of a cone with a value $\mu < 1$ together with each side facet f_j of a cone with $\mu = 1$, *i.e.*, f_j is vertical. Each pair generates the lowest possible angle for this “side j ” of the cone. For each pair, the construction of H_{ij} from Proposition 1 lets us compute this lowest slope. We did check numerically that it is indeed always greater than θ .

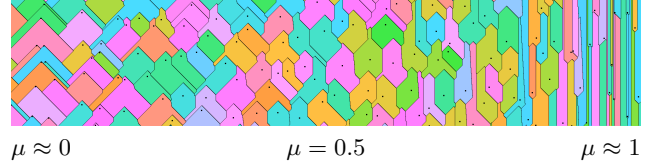


Figure 11: Varying parameter μ with $\theta = 45^\circ$.

Changes in the Voronoi mesh A 2D illustration of how the Voronoi diagram changes is shown in Figure 11. Varying the parameter μ modifies the distribution of the slopes of the facets of the Voronoi diagram, from “all facets have slope θ ” to “most facets are vertical.” Indeed, when $\mu = 0$ every bisector feature are generated by a base facet and have slope θ . When μ is close to 1 the situation is exactly the opposite, most bisector features are generated by side facets resulting in vertical walls.

4.3.4 Varying σ and ζ

The parameters σ and ζ , that control anisotropy and rotation, can vary spatially together; the fabricability is maintained. Indeed, other parameters being fixed, the cones in this 2-parameters family all share the same apex point. As we mentioned before, this implies that a bisector feature generated by side facets of two different cones remains vertical. The features generated by a base facet are the same as in Section 4.2.3.

Changes in the Voronoi mesh Geometrically, as σ decreases, the Voronoi cells become flatter in a direction specified by ζ . This flattening also increases the slope of some bisectors (as we have seen in Section 4.2.3), especially those

parallel to the anisotropy direction. Compare, for example, Figure 9 center and top-right.

4.3.5 Varying σ , ζ , μ and θ

It is possible to vary all four parameters simultaneously. In that case however, μ and θ are interdependent, and function as a single parameter. The supplemental material gives more details. We have not experimented with this 3-parameters family yet, and set it as future work.

4.4 Algorithm and implementation

For fabrication we seek to efficiently generate single slices of the microstructures. In order to print with the smallest available thickness, we produce paths delineating the Voronoi cells – these paths have no thickness, since the thickening comes from the physical material deposition. To guarantee scalability, we devise a procedural approach relying on discretization, as illustrated in Figure 12. We overlay a 2D regular grid over the slice, called the *labels grid* and label each grid square with the site of S closest to the square center, as measured by the polyhedral distance. Then, we extract all the boundary edges between adjacent grid squares with different labels and simplify the extracted jagged paths in order to produce the final deposition paths for fabricating the slice of microstructure. This affords for a simple space-tiling approach, limiting required memory and enabling parallelism.

There are many interesting details on how to implement this efficiently, and we refer the interested reader to the supplemental material. Our implementation uses OpenCL for parallel grid labeling, and C++ for path extraction. On a GeForce GTX 1080 and an Intel i7-6800K, the *Voronoi* labeling for 1000^2 labels takes around 20 ms and the path extraction 1600 ms (the cone parameters are $\theta = 45^\circ$, $k = 8$, $\mu = 0.6$, $\sigma = 1$). The current bottleneck lies in the path extraction since we use an unoptimized sequential method.

We provide in the supplementary material a simple C++ implementation (non-parallel) of grid square labeling.

5 Elastic behavior

We analyze the elasticity of polyhedral Voronoi diagrams with numerical periodic homogenization akin to [34, 31, 23]. Periodic homogenization seeks to find the elasticity tensor characterizing a periodic composite material defined from a unit periodic cell. We do not reproduce here all the details, and refer the interested reader to the aforementioned publications and our supplemental material.

One difference with prior works is that we use the CrAFT software [2], based on the fast Fourier transform (FFT) [28]. In comparison to finite element methods, it allows us to scale to high resolution volumes and to achieve higher precision. CrAFT has been employed by Boittin *et al.* [3] for homogenization of closed-cell Voronoi foams.

After analysis, we consider the parameters of the fitted orthotropic material, primarily the Young’s moduli E_x, E_y, E_z along respectively the x,y and z axis (measure of stiffness). We provide analysis of the shear moduli and Poisson’s ratio in supplemental material, as well as the homogenized tensors obtained by this procedure.

We are also interested in evaluating the overall compressive strength. To do so, we consider the bulk modulus K , that characterizes the tendency of a material to deform in all directions when uniformly loaded in all directions. A high bulk modulus implies higher incompressibil-

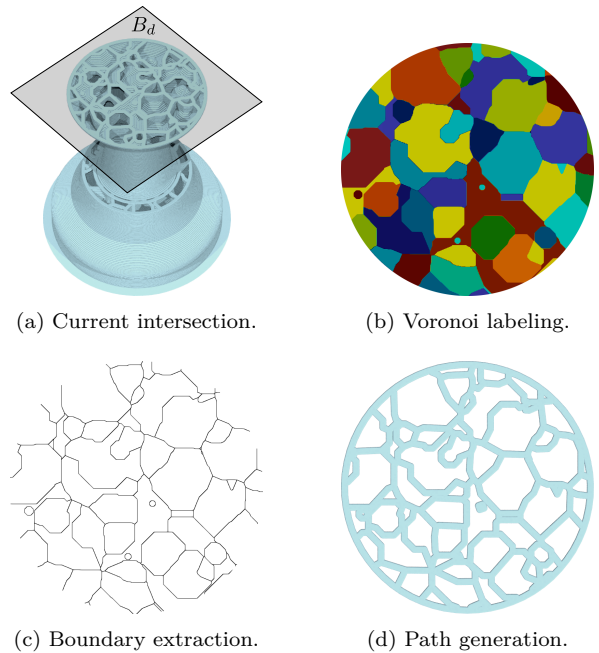


Figure 12: Overview of the path extraction. The input solid C is a bishop chess piece (<https://www.thingiverse.com/thing:378322/>). (a) The bishop cut by the plane B_d . (b) We label each square in the labels grid with its closest site in S . Each Voronoi cell is shown with a different color. (c) We extract the axis-aligned edges between Voronoi cells. (d) We generate simplified deposition paths inside C .

ity. We consider the Voigt-Reuss average of the bulk modulus bounds [7] (details in supplemental material).

All analysis is performed with a base isotropic material with Young’s modulus 1 (normalized) and Poisson’s ratio 0.3. Thus, it is expected that $E_i \in [0, 1]$. However, no bounds exist for the Poisson’s ratio of an orthotropic material [35]. The convergence threshold of CrAFT is set such that the modulus of the divergence of the stress field is lower than 0.005.

5.1 Material space exploration

We explore the material space spanned by the parameterized cone distance (Section 4.2). The unit periodic cell is discretized into 200^3 voxels, we fix the thickness of Voronoi facets to 0.03, and use a point density of 125 point sites per unit cell (given by a $5 \times 5 \times 5$ jittered grid point distribution). We evaluate the Cartesian product of the following cone parameters, for 5 different random realizations of point sites, performing in total 2205 tests:

- $\theta \in \{25^\circ, 45^\circ, 65^\circ\}$
- $\mu \in \{0.2, 0.3, 0.4, 0.5, 0.6, 0.7, 0.8\}$
- $\sigma \in \{1.0, 0.9, 0.8, 0.7, 0.6, 0.5, 0.4\}$
- $k \in \{4, 8, 16\}$

The material space we explored spans a range of relative volumes $\mathcal{V} \in [0.413, 0.634]$ for unit cells. The results for the Young’s moduli are shown in Figure 13, offering a wide range of possibilities along each orthotropy axis. The results for Poisson’s ratio and shear moduli are shown in the supplemental material, spanning a variable range of elastic behaviors, with an always positive Poisson’s ratio.

We observe a good correlation between the cone parameters and the orthotropic elastic constants, as detailed in Section 5.2. In addition, we verified that zero entries of the ideal elasticity orthotropic tensor differ by at most 0.005 from the homogenized one, indicating that an orthotropic material constitutes a plausible approximation.

5.2 Influence of parameters

We now consider how each parameter of the polyhedral distance impacts the mechanical response.

Influence of θ Increasing θ increases further E_z , since the Voronoi facets become closer to being vertical (see Figure 9).

Influence of μ Increasing μ mainly increases E_z , since the area of vertical Voronoi facets increases (see Figure 9). In addition, increasing μ mainly decreases v_{yz} , increases v_{zx} , and decreases G_{yz}, G_{zx} in a different degree depending on θ (see supplemental material).

Influence of σ Decreasing σ decreases E_x and increases E_y, E_z , since the Voronoi facets become comparatively more elongated in the y and z direction than in the x direction (see Figure 9). In addition, decreasing σ mainly increases v_{zx} , decreases v_{xy} , and increases G_{xy} (see supplemental material).

Influence of k We observe that the value of k impacts on the following two properties:

- Increasing k decreases the variance of the homogenized elasticity under different random distributions of the point sites. For each five random realizations with same parameters, the average logarithmic Euclidean distance between any pair of tensors is 11% lower for $k = 8$ (similar for $k = 16$) with respect to $k = 4$.
- Increasing k increases the Voigt-Reuss average bulk modulus. In particular, for $k = 4$ the average unit cell volume is $\mathcal{V} = 0.481$ and $K_{VR} = 0.107$, for $k = 8$ we have $\mathcal{V} = 0.469$ and $K_{VR} = 0.11$. Thus, $k = 8$ exhibits a higher average K_{VR} (similar for $k = 16$) while having an even lower \mathcal{V} .

Thus, a value of $k \geq 8$ is encouraged to achieve better strength to weight ratio, and being closer to the homogenized analysis.

Influence of point density Increasing the point density increases the overall elastic moduli, since the unit cell volume \mathcal{V} increases [6]. This is illustrated in Figure 14.

5.3 Experimental verification

We performed experimental verification of the predicted elastic behavior. We print three samples with varying orthotropy and measure their linear elastic response (Young’s modulus) using a compression test along each axis. The results are reported in Figure 16. To mitigate the impact of the choice of printer, we use three different machines (see Figure for details).

The experimental results are consistent with numerical results, even though there are differences. The main one is a lower stiffness along the build direction, on average. This is to be expected since layered materials are anisotropic.

As future work, we would like to investigate homogenization with an anisotropic material for AM [18]. Nevertheless, the discrepancies are limited and we observe a direct correlation between control parameters (μ, σ) and the measured Young’s moduli. We provide curves for one sample in Figure 17, revealing the non-linear behavior under large compressions. The curve reveals a smooth response with the expected flattening. We also performed a repeatability test, taking five measurements along each axis of a same sample. We observe variations of $\pm 3\%$ without any noticeable trend.

5.4 Comparison to tessellations by planes

Self-supported structures made of interleaved sets of parallel planes have become a popular choice for filling volumes in the context of FFF [17, 38, 15].⁴ To the best of our knowledge, the material space spawned by these infills has not been studied in the context of microstructures. Nevertheless, we provide here some elements of comparison.

A first important limitation of rhombic structures is that they cannot be graded spatially in orientation or anisotropy, due to their regular structure. Therefore, they offer significantly less control than our approach. Their density can be varied by subdivision, for instance maximizing rigidity [38]. However, as illustrated in Figure 24, grading by subdivision introduces sudden jumps that impair the smoothness of the final elastic behavior.

Figure 15 compares the bulk modulus of the structures, for the two typical cases of using three or four sets of parallel planes. Rhombic structures are 20% stiffer for a same volume, but this advantage vanishes if orthotropy is desired: our structures become significantly stiffer in the preferred directions for a same volume.

The rhombic structures, thanks to the use of straight lines, print slightly faster than our structures (14% difference on a Prusa3 on default settings, may vary with acceleration settings).

6 Applications

In this section we present several designs modeled with our technique. The control fields are created either through a dedicated painting interface, or procedurally (we use a domain specific language for this purpose).

The designs we present are illustrations, demonstrating the versatility of our technique. To reveal the foam we print them without an external perimeter – this means that some small unsupported regions on the sides exists. In practice we observe no detrimental impact. Real designs could add an external thin skin where needed.

A striking difference between our designs and those produced with SLA/SLS is the ease of production – thanks to the use of FFF printers – as well as the robustness of the final part. In particular, parts printed with filaments having varying degrees of elasticity (Ninjatek *SemiFlex* and *Cheetah*) can flex very significantly without breaking. In our experience, foams are much more difficult to produce on SLA printers, require a careful choice of printer and parameters [40] and are more fragile after curing.

Our first example is a bar with varying orthotropy, shown in Figure 18. An abrupt change in orthotropy direction in the middle of the bar triggers very different behavior on both sides.

⁴See also cubic/tetrahedral infill in software *Cura*.

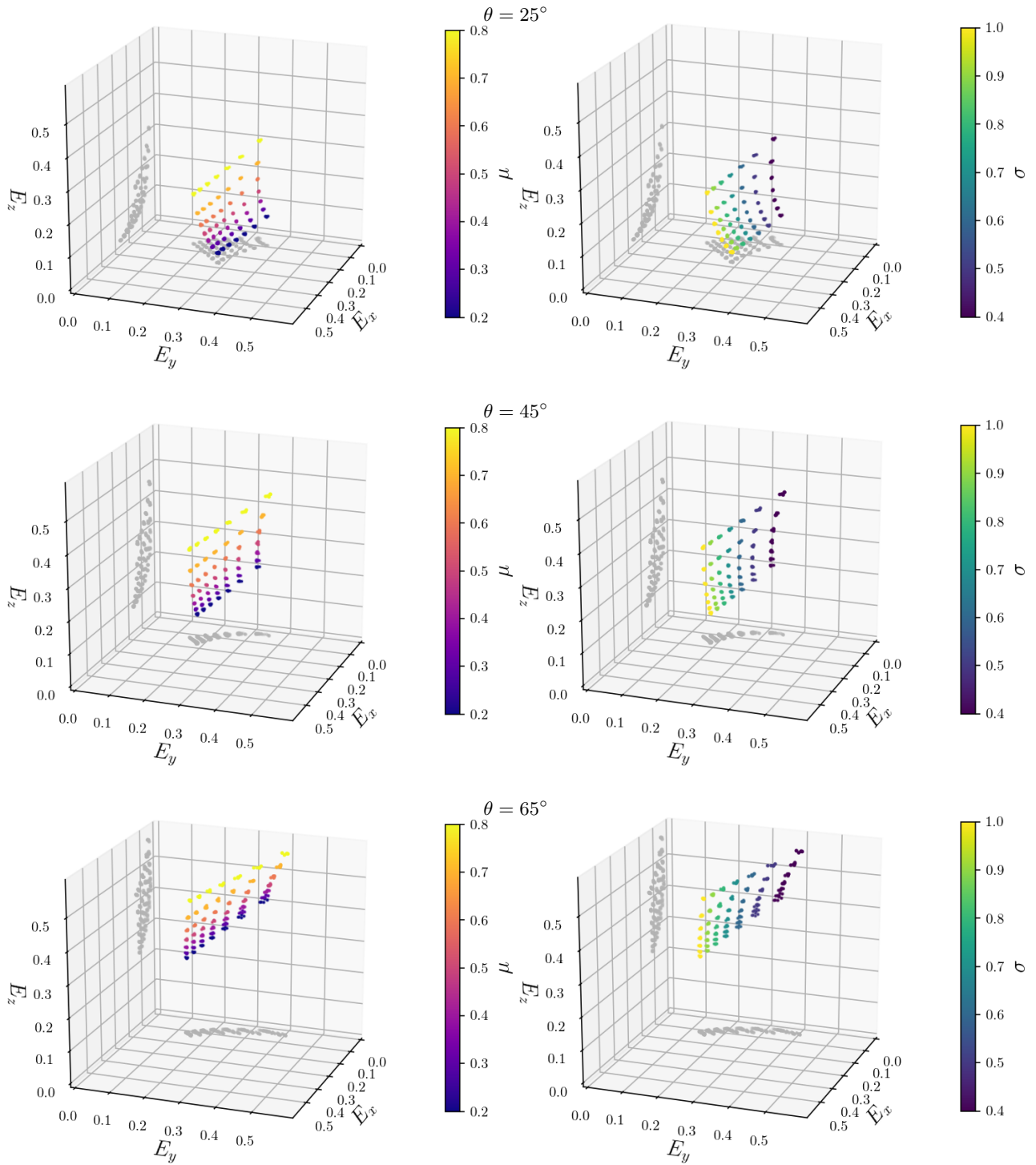


Figure 13: Material space for $k = 8$. Each row corresponds to a different minimal bisector slope θ . Each plot dot denotes a single test. The plot axes correspond the three orthogonal Young’s moduli. The color of dots either depicts μ (left column) or σ (right column). For better interpretation, each dot is projected in gray color to the E_z and E_y planes.

Our second example is a cylinder with a direction of orthotropy that rotates 90 degrees along the main axis, shown Figure 19. This creates an interesting case where, under rotation in the proper orientation, the cylinder twists and flatten across its section. It is otherwise rigid vertically.

Our third example is an illustration of a prosthetic finger, reproducing a result from [23]. The two joints are obtained by a strong orthotropy aligned with the joint “axis.” Density also varies between the outside (denser) and the inside of the bend. The result offers a preferred direction of flex that corresponds better to a natural joint, in particular it

is harder to bend sideways (by orthotropy) or reverse (by density). See Figure 20.

Our fourth example is a wheel that can be mounted on an actual RC car (a *Monster Beetle* by *Tamiya*), see Figure 21. The wheel prints as a single part, is lighter than the original (109g versus 130g), and deforms radially (shock absorbent). Of course, the design would have to be refined to act as an efficient tire. Our technique makes such applications accessible to hobbyists.

Our fifth example, Figure 22, illustrates how orthotropy can be arranged radially to achieve different properties in

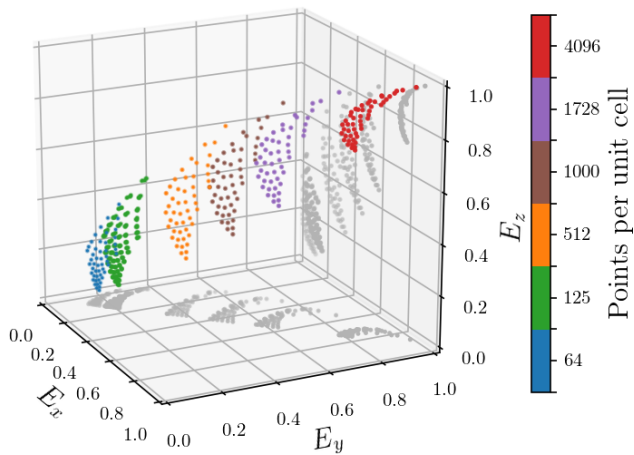


Figure 14: Material space for $k = 8$ and $\theta = 45^\circ$. We consider the same range of parameters σ and μ used in Figure 13, while varying in addition the point density for $\{64, 125, 512, 1728, 4096\}$ point sites per unit cell. The data for 125 point sites per unit cell (green points) corresponds exactly to $\theta = 45^\circ$ in Figure 13 (middle row). For better interpretation, each dot is projected in gray color to the E_z and E_y planes.

a pipe design.

Our final example is a shoe sole with controlled elasticity, shown in Figure 23. By modifying density, angle and anisotropy we are able to control both the “softness” and “bending” of the sole. While this is a purely illustrative example, we hope our method will help produce orthopaedic footwear at much lower price points than those produced on high end SLS/SLA printers.

7 Limitations, future work

To the best of our knowledge, the presented microstructures form the first metamaterial that is well suited for FFF and offers a wide range of controllable elastic behaviors. Their properties can be graded following custom control fields, while still satisfying strict guarantees on manufacturability.

There are however a number of limitations and areas of improvement. In terms of overall rigidity (bulk modulus), our structures are less effective than plane tessellations (see Figure 15). It remains an open question whether there exists other polyhedral distances that improve bulk modulus, while still enforcing the fabrication constraints.

The stochastic geometry has an impact on printing speed (about 15% slower than straight line infill on our printers). This possibly could be mitigated by optimizing the traversal of the paths; our slicer currently uses a simple “go to next closest path” heuristic.

A minor issue related to design is that the point sites are not always close to the centroid of the Voronoi cell. Therefore, at low densities and high anisotropy, there can be an offset between the control field and its actual effect of the structure. It would be interesting to compensate for this.

Finally, while we efficiently extract slices, we did not investigate interactive visualization of the microstructures – one possible approach is ray-marching. Efficient ray-traversal of the structures is an interesting topic for future work.

8 Conclusions

By carefully choosing the distance functions used to model Voronoi diagrams, we are able to produce stochastic closed-cell foams that enforce all manufacturability constraints on continuous deposition processes. We proposed a parameterized polyhedral distance based on cones, that provides good correlation between well understood geometric properties and observed elastic behaviors.

We envision that our method could also be helpful in optimizing periodic microstructures [34, 31] since it provides a space of geometric structures that are certain to be fabricable. It may also be interesting to use it as a replacement in approaches that optimize Voronoi diagrams for additive manufacturing, such as the work of Lu *et al.* [20].

There is no direct way to interpret our structures as open-cell foams. The Voronoi edges could be considered but they do not enforce fabrication constraints. Therefore, our technique is complementary to existing works targeting powder and resin based systems, as it answers the need for parameterized metamaterials applicable to continuous deposition.

Acknowledgments We thank Noémie Vennin and Jimmy Etienne for their help in designing and printing results. This work was supported by ERC⁵ grant ShapeForge (StG-2012-307877), Région Lorraine and FEDER.⁶

References

- [1] BOISSONNAT, J.-D., SHARIR, M., TAGANSKY, B., AND YVINEC, M. Voronoi diagrams in higher dimensions under certain polyhedral distance functions. In *Proceedings of the Eleventh Annual Symposium on Computational Geometry* (1995), pp. 79–88.
- [2] BOITTIN, G., GARAJEU, D., LABÉ, A., MOULINEC, H., SILVA, F., AND SUQUET, P. Craft, 2014.
- [3] BOITTIN, G., VINCENT, P.-G., MOULINEC, H., AND GĂRĂJEU, M. Numerical simulations and modeling of the effective plastic flow surface of a biporous material with pressurized intergranular voids. *Computer Methods in Applied Mechanics and Engineering* 323, Supplement C (2017), 174 – 201.
- [4] CHEW, L. P., AND DYRSDALE, III, R. L. S. Voronoi diagrams based on convex distance functions. In *Proceedings of the First Annual Symposium on Computational Geometry* (1985), pp. 235–244.
- [5] CORBALAN, A., MAZON, M., AND RECIO, T. Geometry of bisectors for strictly convex distances. *International Journal of Computational Geometry & Applications* 06, 01 (1996), 45–58.
- [6] GIBSON, L. J., AND ASHBY, M. F. *Cellular solids: structure and properties*. Cambridge university press, 1999.
- [7] HILL, R. The elastic behaviour of a crystalline aggregate. *Proceedings of the Physical Society. Section A* 65, 5 (1952), 349.
- [8] HORNUS, S., LEFEBVRE, S., DUMAS, J., AND CLAUX, F. Tight printable enclosures and support structures

⁵ European Research Council

⁶ Fond européen de développement régional

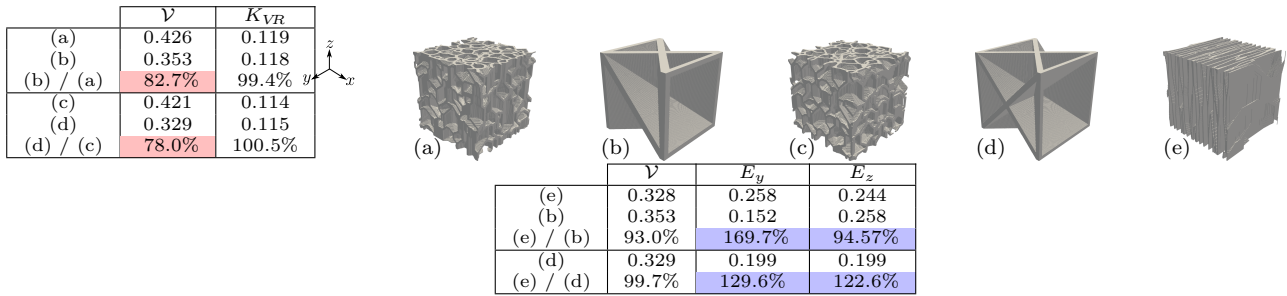


Figure 15: We compare infills made of tessellations made of planes with polyhedral Voronoi diagrams. We set a minimal slope of $\theta = 45^\circ$ for all tests. We give in the supplemental material the full expression of the homogenized elasticity tensors of each test. *Left table:* We determine the volume \mathcal{V} required to achieve similar K_{VR} values (± 0.001). Since polyhedral Voronoi diagrams span a wide space of material, we select the closest sample (with respect to K_{VR}) in the database of Figure 13. However, note that other samples having similar K_{VR} are possible. (a) and (c) correspond, respectively, to the closest match for (b) and (d). As seen in the third and sixth row, our infills require 20% more material for the same K_{VR} . *Right table:* When orthotropy is desired, for instance to mimic a laminate much stiffer in y, z than in x , polyhedral Voronoi diagrams are better suited. As seen in the third row, for a lower volume (e) is significantly more stiff in y than (b), while in the fifth row (e) is significantly stiffer in both y, z than (d) for a similar volume.

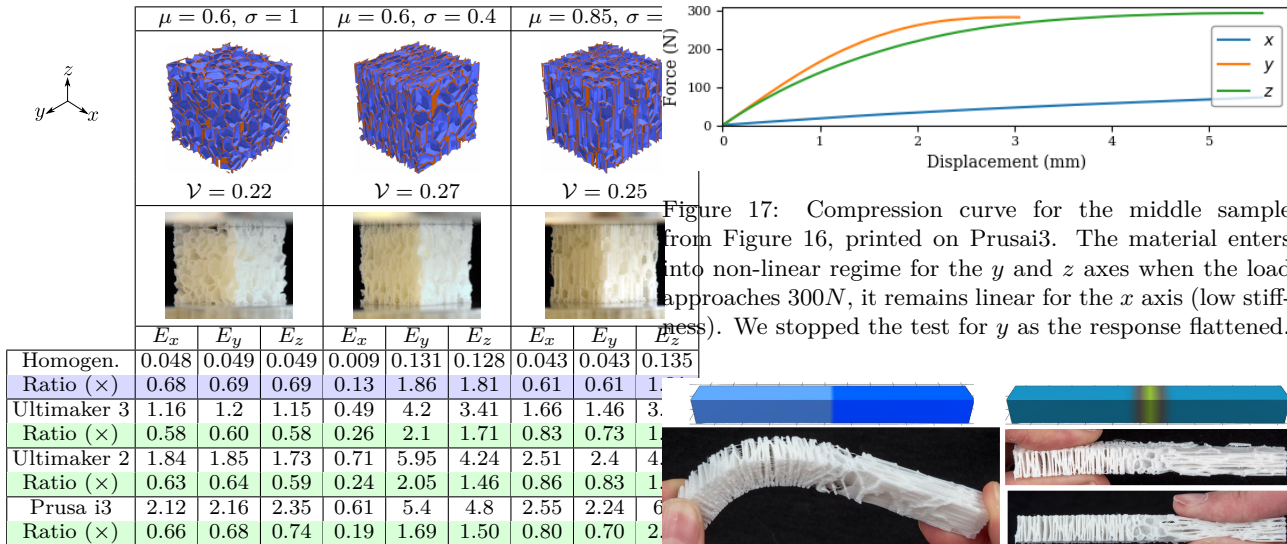


Figure 17: Compression curve for the middle sample from Figure 16, printed on Prusai3. The material enters into non-linear regime for the y and z axes when the load approaches 300N, it remains linear for the x axis (low stiffness). We stopped the test for y as the response flattened.

Figure 16: Comparison between numerical homogenization (Young's moduli in the normalized range $[0, 1]$) and experimental compression tests performed on an Instron 3345 testing machine. Experimental Young's moduli are given in megapascals (MPa). For all three tests we set $k = 8$ and $\theta = 45^\circ$, and we vary μ and σ . We have printed each sample (30 mm cubes) on three different printers (Ultimaker 3, and Ultimaker 2, and Prusa i3) using different rolls of filaments (Ninjatek *Semiflex*) in diameters of either 1.75 mm (Prusai3) or 2.85 mm (Ultimakers), with the same layer thickness (0.2 mm) and print speed (15 mm/sec). We apply a compression test to each direction, to obtain E_x , E_y , and E_z . For comparison we compute ratios to the average value across all nine tests of the *same* printer (i.e. how much more rigid/flexible each is with respect to the average). As can be seen the ratios agree well overall. We provide in the supplemental material the full expression of the homogenized elasticity tensor of each compression test.

Figure 18: *Top row:* Orientation field ζ (left) and anisotropy field σ (right). *Pictures, bottom row:* The left side bends easily while the right side remains rigid. On the contrary the right side can be compressed sideways (bottom image), while the left side is much more rigid (top image).

distance functions in 3D. In *Proceedings of the Thirty-third Annual ACM Symposium on Theory of Computing* (2001), pp. 316–321.

[9] ICKING, C., AND HA, L. A tight bound for the complexity of voronoi diagrams under polyhedral convex for additive manufacturing. In *Proceedings of the Eurographics Workshop on Graphics for Digital Fabrication* (2016), GraDiFab '16, pp. 11–21.

[10] ICKING, C., KLEIN, R., LÉ, N.-M., AND MA, L. Convex distance functions in 3-space are different. *Fundamenta Informaticae* 22, 4 (1995), 331–352.

[11] ICKING, C., KLEIN, R., MA, L., NICKEL, S., AND WEISSLER, A. On bisectors for different distance functions. *Discrete Applied Mathematics* 109, 1 (2001), 139–161.

[12] ION, A., FROHNHOFEN, J., WALL, L., KOVACS, R., ALISTAR, M., LINDSAY, J., LOPES, P., CHEN, H.-T., AND BAUDISCH, P. Metamaterial mechanisms. In *Proceedings of the 29th Annual Symposium on User Interface Software and Technology* (New York, NY, USA, 2016), UIST '16, ACM, pp. 529–539.



Figure 19: Cylinder with varying direction of orthotropy (from 0 to 90 degrees between the handles), vertically rigid but allowing rotation in one direction.



Figure 20: The articulations of this finger prosthetic are obtained by spatially varying density and anisotropy. The design is very robust and easy to print: it uses a rubber-like filament (*Cheetah* by *NinjaTek*) printed on a standard FFF printer (Prusa3).

- [13] KLEIN, R., AND WOOD, D. *Voronoi diagrams based on general metrics in the plane*. Springer Berlin Heidelberg, 1988, pp. 281–291.
- [14] LEARY, M., BABAEE, M., BRANDT, M., AND SUBIC, A. Feasible build orientations for self-supporting fused deposition manufacture: A novel approach to space-filling tessellated geometries. *Advanced Materials Research* 633 (2013), 148–168.
- [15] LEE, J., AND LEE, K. Block-based inner support structure generation algorithm for 3d printing using fused deposition modeling. *The International Journal of Advanced Manufacturing Technology* 89, 5 (2017), 2151–2163.
- [16] LEE, M., FANG, Q., RYU, J., LIU, L., AND KIM, D.-S. Support-free hollowing for 3D printing via voronoi diagram of ellipses. *Arxiv* (2017).
- [17] LEFEBVRE, S. 3D infilling: faster, stronger, simpler, 2015. <http://sylefeb.blogspot.fr/2015/07/3dprint-3d-infilling-faster-stronger.html>.
- [18] LIU, X., AND SHAPIRO, V. Homogenization of material properties in additively manufactured structures. *Computer-Aided Design* 78, Supplement C (2016), 71–82.
- [19] LIVESU, M., ELLERO, S., MARTÍNEZ, J., LEFEBVRE, S., AND ATTENE, M. From 3D models to 3D prints: An overview of the processing pipeline. *Computer Graphics Forum* (2017).

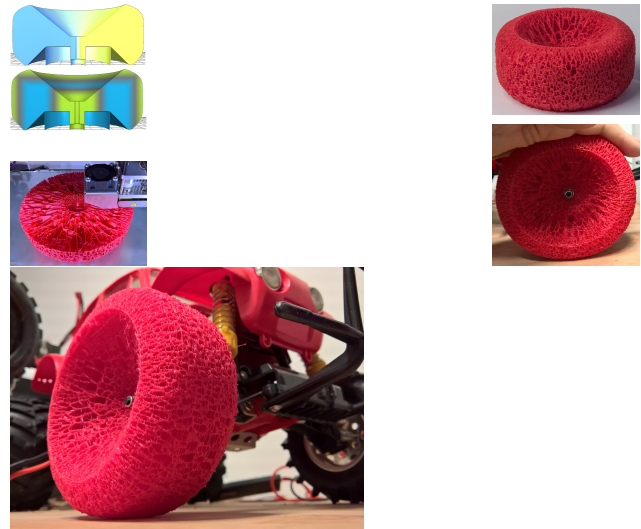


Figure 21: *Top left*: Orientation field ζ (top) and density field (below). The anisotropy is constant at $\sigma = 0.3$. *Bottom left*: Wheel being printed on an Ultimaker 2 with *Semiflex* filament at 0.3 mm thickness. The print took 19 hours. *Middle column*: The finished wheel and its deformation under load. *Right*: Ready to run!

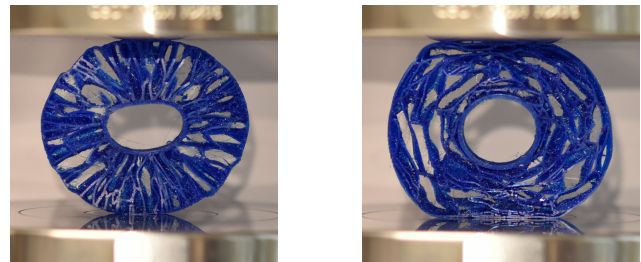


Figure 22: Illustration of an application to pipe design. The left design transfers forces between the inner and outer pipes, while the right design protects the inner pipe from external forces. The designs differ only by the orthotropy angle.

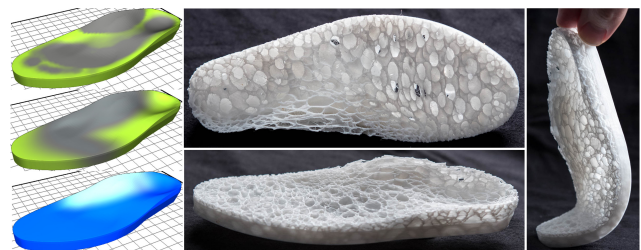


Figure 23: A 3D printed shoe sole. *Left*: Control fields used on the model, density (top), orthotropy strength (middle) and angle (bottom). *Right*: Printed shoe, top, side and bending. The shoe is printed without any skin to reveal the foam structure.

- [20] LU, L., SHARF, A., ZHAO, H., WEI, Y., FAN, Q., CHEN, X., SAVOYE, Y., TU, C., COHEN-OR, D., AND CHEN, B. Build-to-last: Strength to weight 3d printed objects. *ACM Trans. Graph.* 33, 4 (July 2014), 97:1–97:10.
- [21] LUXNER, M. H., STAMPFL, J., AND PETTERMANN, H. E. Numerical simulations of 3D open cell structures – influence of structural irregularities on elasto-

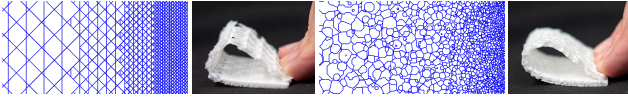


Figure 24: Compared to subdividing rhombic infill (left), Voronoi polyhedral diagrams produce a smoother grading (right) without marked transitions, triggering a smoother elastic behavior. Both structures use the same amount of material. Ours printed 14% slower due to a more complex geometry.

- plasticity and deformation localization. *International Journal of Solids and Structures* 44, 9 (2007), 2990 – 3003.
- [22] MA, L. *Bisectors and Voronoi diagrams for convex distance functions*. PhD thesis, Fernuniversität, Fachbereich Informatik, 2000.
- [23] MARTÍNEZ, J., DUMAS, J., AND LEFEBVRE, S. Procedural voronoi foams for additive manufacturing. *ACM Trans. Graph.* 35, 4 (2016), 44:1–44:12.
- [24] MARTÍNEZ, J., SONG, H., DUMAS, J., AND LEFEBVRE, S. Orthotropic k-nearest foams for additive manufacturing. *ACM Transactions on Graphics* 36, 4 (July 2017), 121:1–121:12.
- [25] MARTINI, H., AND SWANEPOEL, K. The geometry of Minkowski spaces – a survey. part II. *Expositiones Mathematicae* 22, 2 (2004), 93 – 144.
- [26] MCMAINS, S., SMITH, J., WANG, J., AND SEQUIN, C. Layered manufacturing of thin-walled parts. In *ASME Design Engineering Technical Conference, Baltimore, Maryland* (2000).
- [27] MEDEIROS E SÁ, A., MELLO, V. M., RODRIGUEZ ECHAVARRIA, K., AND COVILL, D. Adaptive voids. *The Visual Computer* 31, 6 (2015), 799–808.
- [28] MOULINEC, H., AND SUQUET, P. A numerical method for computing the overall response of nonlinear composites with complex microstructure. *Computer Methods in Applied Mechanics and Engineering* 157, 1 (1998), 69–94.
- [29] OKABE, A., BOOTS, B., SUGIHARA, K., AND CHIU, S. N. *Spatial Tessellations: Concepts and Applications of Voronoi Diagrams*. John Wiley & Sons, 2009.
- [30] PANETTA, J., RAHIMIAN, A., AND ZORIN, D. Worst-case stress relief for microstructures. *ACM Transactions on Graphics* 36, 4 (2017), 122:1–122:16.
- [31] PANETTA, J., ZHOU, Q., MALOMO, L., PIETRONI, N., CIGNONI, P., AND ZORIN, D. Elastic textures for additive fabrication. *ACM Trans. Graph.* 34, 4 (2015), 135:1–135:12.
- [32] PASKO, A., FRYAZINOV, O., VILBRANDT, T., FAYOLLE, P.-A., AND ADZHIEV, V. Procedural function-based modelling of volumetric microstructures. *Graphical Models* 73, 5 (2011), 165–181.
- [33] ROBERTS, A., AND GARBOCZI, E. Elastic properties of model random three-dimensional open-cell solids. *Journal of the Mechanics and Physics of Solids* 50, 1 (2002), 33 – 55.
- [34] SCHUMACHER, C., BICKEL, B., RYS, J., MARSCHNER, S., DARAIO, C., AND GROSS, M. Microstructures to control elasticity in 3D printing. *ACM Trans. Graph.* 34, 4 (2015), 136:1–136:13.
- [35] TING, T., AND CHEN, T. Poisson’s ratio for anisotropic elastic materials can have no bounds. *The quarterly journal of mechanics and applied mathematics* 58, 1 (2005), 73–82.
- [36] VIDIMČE, K., WANG, S.-P., RAGAN-KELLEY, J., AND MATUSIK, W. OpenFab: A programmable pipeline for multi-material fabrication. *ACM Trans. Graph.* 32, 4 (2013), 136:1–136:12.
- [37] WANG, W., LIU, Y. J., WU, J., TIAN, S., WANG, C. C. L., LIU, L., AND LIU, X. Support-free hollowing. *IEEE Transactions on Visualization and Computer Graphics* (2017).
- [38] WU, J., WANG, C. C., ZHANG, X., AND WESTERMANN, R. Self-supporting rhombic infill structures for additive manufacturing. *Computer-Aided Design* 80 (2016), 32–42.
- [39] XIE, Y., AND CHEN, X. Support-free interior carving for 3D printing. *Visual Informatics* 1, 1 (2017), 9–15.
- [40] ZHOU, Q. A study in fabricating microstructures, 2015. <https://medium.com/3d-printing-stories/a-study-in-fabricating-microstructures-part-1-f267d2983266>
- [41] ZHU, B., SKOURAS, M., CHEN, D., AND MATUSIK, W. Two-scale topology optimization with microstructures. *ACM Trans. Graph.* 36, 5 (July 2017), 164:1–164:16.

Polyhedral Voronoi diagrams for additive manufacturing, Supplemental material

Jonàs Martínez, Samuel Hornus, Haichuan Song, Sylvain Lefebvre
Inria

January 20, 2018

Polyhedral Voronoi diagrams and algorithm

In Section 1 we provide the rationale behind the construction of Polyhedral bisectors (Section 1.1), how to find the normal of bisector facets (Section 1.2), and how to identify any bisector local minima that may violate fabrication constraints (Section 1.3).

In Section 2, we detail a 3-parameters family of cone distances that satisfy the fabrication constraints but that we have not experimented with yet.

In Section 3, we explain how we compute the labels in the labels grid. The details are important for obtaining a reasonably efficient implementation.

Elastic behavior

In Section 4, we give the analytic expressions for the orthotropic compliance tensor and the bulk modulus bounds.

Sections 5 and 6 provide the elasticity tensors for Figures 15 and 16 in the article.

In Figure 3 and Figure 4 we provide the Poisson's ratio and shear modulus, respectively, of Figure 13 in the article.

1 Constructions

We say that two features $X \subset P$ and $Y \subset P$ on the boundary of the distance polytope P generate a feature B of the bisector $\mathcal{B}(p, q)$ when

$$B = \{(p + \lambda X) \cap (q + \lambda Y) \mid \lambda > 0\}. \quad (1)$$

B is empty or not depending on the relative position of the point sites p and q .

1.1 Construction of a bisector

Given two point sites p and q , let us define the unit vector $u = \frac{q-p}{\|q-p\|}$. The facets of P can be partitioned into front and back facets, where the normal vector of a front (resp. back) facet has a non-negative (resp. non-positive) dot-product with u . A point r on the bisector $\mathcal{B}(p, q)$ can be written as $r = p + \lambda r_i = q + \lambda r_j$ where $\lambda = d_P(p, r) = d_P(q, r)$, r_i is a point of a front-facet of P , r_j is a point of a back-facet of P and the line $(r_i r_j)$ is also parallel to the vector u . Conversely, given a point r_i on a front-facet and a point r_j on a back-facet; if both points also lie on a line parallel to u , then they generate (in the sense given above) exactly one point on the bisector. This proves that the bisector $\mathcal{B}(p, q)$ can be constructed from the overlay O of the projections of the front facets and the back facets on a plane orthogonal to vector u , through a function $\phi : O \mapsto \mathcal{B}(p, q)$: Let v be a vertex of a cell of the overlay. The points $r_i(v)$ and $r_j(v)$ are computed as the intersection of P with the line through v parallel to the vector u . These two points on P generate the bisector point $\phi(v) = p + \lambda(v)r_i(v) = q + \lambda(v)r_j(v)$ where $\lambda(v) = \frac{\|q-p\|}{\|r_i(v) - r_j(v)\|}$.

Once the vertices of the bisector are computed, its facets are trivially obtained since they follow the same combinatorics as the overlay. Finally, silhouette vertices on the boundary of the overlay are mapped to bisector points at infinity.

The present submission comes with a compiled javascript interactive visualization of the polyhedral bisector. The reviewer is invited to check the “bisector/” directory and the “README.txt” file in the parent directory.

1.2 Normal vector of a bisector facet

Let f be a facet of the bisector $\mathcal{B}(p, q)$ generated by the facets f_i and f_j of P . (In particular, the projections of both facets on a plane orthogonal to $q - p$ have a non-empty intersection, which is a cell of the overlay mentioned in Section 1.1.) Let n_i be the outward normal vector to facet f_i . Let $\alpha_i > 0$ be the distance from the origin to the plane H_i supporting f_i . In particular, if r_i is a point of f_i then $\alpha_i = r_i \cdot n_i$.

Proposition 1 ([6]). *Write H_{ij} for the plane that spans the origin and the line $H_i \cap H_j$. The bisector facet f (generated by f_i and f_j) is parallel to the plane H_{ij} and its normal vector is proportional to $\alpha_j n_i - \alpha_i n_j$.*

Proof. We prove the formula for the normal vector. Let $r_i \in f_i$ and $r_j \in f_j$ be the pair of features that generates a point $\phi(v)$ where v is any point on the line $(r_i r_j)$. We have

$$\begin{aligned} \phi(v) \cdot (\alpha_j n_i) &= (p + \lambda(v)r_i) \cdot (\alpha_j n_i) & (2) \\ &= K + \lambda(v)\alpha_j(r_i \cdot n_i) = K + \lambda(v)\alpha_j\alpha_i & (3) \end{aligned}$$

$$\begin{aligned} \text{and } \phi(v) \cdot (\alpha_i n_j) &= (q + \lambda(v)r_j) \cdot (\alpha_i n_j) & (4) \\ &= K' + \lambda(v)\alpha_i(r_j \cdot n_j) = K' + \lambda(v)\alpha_i\alpha_j, & (5) \end{aligned}$$

$$\text{with } K = \alpha_j n_i \cdot p \quad (6)$$

$$\text{and } K' = \alpha_i n_j \cdot q. \quad (7)$$

We see that $\phi(v) \cdot (\alpha_j n_i - \alpha_i n_j)$ is a constant for any point v in the given overlay cell. \square

1.3 Finding a local minimum

Let e be a directed line segment on P (for example, an edge, but not necessarily; we see e also as a vector). Let f_i a facet of P not parallel to e , with outward normal vector n_i . Then for some directions $p - q$, segment e and facet f_i do generate a line segment e' on the bisector $\mathcal{B}(p, q)$. Let l and l' be the lines supporting segments e and e' respectively. Then l' is parallel to the line from the origin to the point $x = l \cap H_i$. As a point walks along e , the corresponding bisector point walks along e' in the direction x if $e \wedge n_i > 0$, and in the opposite direction, $-x$, otherwise.

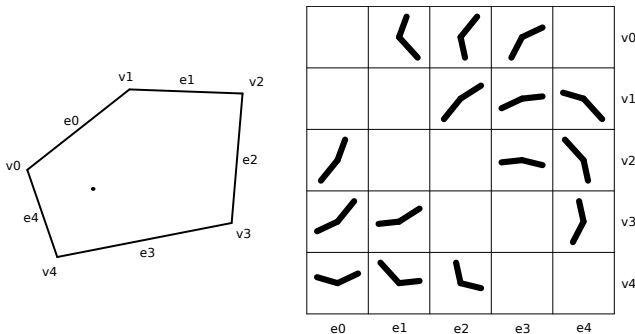


Figure 1: The 15 possible bisector vertex configurations induced by a 5 sided polygon P , corresponding to all the possible interactions between edges (horizontal axis) and vertices (vertical axis) of P . Vertex v_4 generates two local minimum configurations with edges e_0 and e_1 . Therefore the particular polyhedral distance induced by this polygon does not produce fabricable Voronoi diagrams.

A vertex v of the bisector $\mathcal{B}(p, q)$ is the image through ϕ of a vertex of the overlay O . Thus, vertex v is generated either by a vertex v_i and a facet f_j of P (that can not contain v_i) or by two edges e_i and e_j of P . In either case, the argument above lets us compute the directions (in \mathbb{R}^3) of each bisector edge emanating from v . If the z -component of every direction is positive, then v is a local minimum. This gives an algorithm to decide in quadratic time whether or not a distance polytope can produce local minimum in the derived polyhedral Voronoi diagram. Figure 1 shows all the bisector vertex configurations for a 2D polygonal distance.

2 Varying σ , ζ , μ and θ

If we increase θ , then ℓ decreases and the apex moves down. We can take it back up to its original position by also increasing μ . We then obtain a 3-parameters family of cones whose parameters can spatially vary together and independently while respecting both fabrication constraints. Parameters θ (represented by $\ell = \tan(\pi/2 - \theta)$) and μ are related by

$$\ell^2 = \frac{A_z^2}{\mu^2} - (1 + A_z)^2. \quad (8)$$

Changes in the Voronoi mesh When increasing θ , the bisector facets generated by a side facet and the base facet of the distance cone become more vertical. Then, to compensate the lowering of the apex, we also increase μ according to Equation (8). We also expect this compensation to raise the slope of the bisector facets (Main paper, Section 4.3.3). Therefore, we can interpret the μ - θ pair as working in tandem for us to tune the stiffness in z . In the horizontal plane, we can still choose σ and ζ at will to control horizontal stiffness.

3 Algorithmic details

Let $C \subset \mathbb{R}^3$ be the input solid to be filled with our microstructure mesh \mathcal{K} . In a slice at height d , the deposition paths that form the microstructure are given by $B_d \cap \mathcal{K} \cap C$. Since \mathcal{K} is piecewise linear, $B_d \cap \mathcal{K}$ is composed of a set of line segments.

A sweep-plane approach to compute $B_d \cap \mathcal{K}$ would be ideally suited for our setting since we do want to extract many horizontal slices of \mathcal{K} . Such an algorithm involves updating

the planar topology of $B_d \cap \mathcal{K}$ as d varies monotonously. Dehne *et al.* [3] studied the two dimensional setting of the wavefront approach for convex metrics. In the same vein, Chen *et al.* [2] presented a sweep-line algorithm for certain polygonal metrics in the plane. However, to the best of our knowledge there exists no work dealing with the three-dimensional case. This is mostly due to the complicated update of the sweep-plane, and the difficulties in obtaining a robust implementation [2].

Instead, we propose a simpler discretized approach to approximate the deposition paths, that we illustrate in Figure 12. We overlay a 2D regular grid over $C \cap B_d$, called the *labels grid* and label each grid square with the site of S closest to the square center, as measured by the polyhedral distance d_P . Then, we extract all the boundary edges between adjacent grid squares with different labels and simplify the extracted jagged paths in order to produce the final deposition paths for fabricating the microstructure inside C .

The *labels grid* should not be confused with the 3D *sites grid*, defined in Section 4.3.1: the labels grid is 2D and much denser.

3.1 Voronoi labeling

This section describes the labeling of each square of the 2D labels grid. The size of each such square should be much smaller than the size of the finest cells of the sites grid. In our experiments, it is set from $20 \mu\text{m}$ to $100 \mu\text{m}$. The labels grid samples the horizontal plane B_d at height $z = d$. For a given grid square center point c , we need to compute the point site $\nu(c) \in S$ closest to c , that will serve as a label for that square. (Note that the query point c is located in \mathbb{R}^3 and $c_z = d$.) Let s_c be the cell of the sites grid that contains the query c . To find $\nu(c)$ efficiently, we traverse a pre-computed list of cells around s_c : $\nu(c) = \operatorname{argmin}_{s \in s_p + \Sigma} d_P(s, c)$. The list Σ stores 3D indices *relative* to the reference cell C_0 with index $(0, 0, 0)$ and is sorted by distance to C_0 . The computation of Σ is detailed below.

3.2 Computation of Σ with a uniform distance

The idea is to obtain an upper bound λ_{\max} on the distance between the query point c and its nearest site $\nu(c)$ and then store in Σ the indices of all the cells that are at distance no greater than λ_{\max} from the reference cell C_0 .

Recall that the distance d_P is not symmetric. Since we want to center the search around the query point c , we make the following observation. Writing P' for the reflection of P with respect to the origin, we have $d_P(s, c) = d_{P'}(c, s)$ and $\forall \lambda \geq 0, d_P(s, c) \leq \lambda \iff c \in s + \lambda P \iff s \in c + \lambda P'$. We are then guaranteed that $\nu(c)$ lies inside $c + \lambda_{\max} P'$, which lets us restrict the search.

To compute the upper bound λ_{\max} for our specific point site distribution (Section 4.3.1), we use the following property: If we can fit an axis-aligned cube of side length $2a$ into the scaled unit-ball λP for some $\lambda > 0$ (Figure 2-left), then we have the guarantee that *any* translate of λP (or of $\lambda P'$, in particular, $c + \lambda P'$) contains at least one cell of a regular grid whose cells have side length a (Figure 2-middle). If s is a point site in that cell, then $s \in c + \lambda P' \iff d_P(s, c) \leq \lambda$. From the particular geometry of the unit-ball that we use (a polyhedral cone, Section 4.2), we can (conservatively) fit a cube touching the base of the cone and of side length $L = \frac{(1+A_z)\sqrt{2}\ell}{1+A_z+\sqrt{2}\ell}$ where $1+A_z$ is the height of the cone and $\ell/\cos(\pi/k)$ is the radius of its base for some integer $k \geq 3$. Thus, if the sites grid cells have side-length a , the nearest

site of any query point is at polyhedral-distance no more than $\lambda_{\max} = \frac{2a}{L}$ from the query. (In our implementation, we scale the problem so that $a = 1$.)

Using a breadth-first traversal starting at C_0 , we pre-compute the search list Σ of cell indices (in the sites grid). The search-list is truncated when the distance reaches λ_{\max} .

Remark Our “jittered grid” site distribution scheme gives us an easy-to-compute upper bound on the distance from any query point in \mathbb{R}^3 to the nearest point site in S . Nonetheless, such an upper bound can also be derived for other point sampling schemes and used in our technique.

Computing distances The distance $d_{P'}$ between a point and an axis-aligned cubical cell is computed efficiently using a simple modification of Greene’s technique [4]. During the computation of the search-list, one needs to compute the polyhedral distance between two grid cells:

$$d_{P'}(C_0, C) = \min\{\lambda : \exists a \in C_0, \exists b \in C, b \in a + \lambda P'\} \quad (9)$$

$$= \min\{\lambda : \exists p \in (C \ominus C_0), p \in \lambda P'\} \quad (10)$$

$$= d_{P'}(O, C \ominus C_0). \quad (11)$$

where O is the origin and $C \ominus C_0 = \{b - a : a \in C_0, b \in C\}$ is a cube twice the size of C or C_0 . Since we stop the construction of the search list Σ when the distance gets larger than λ_{\max} , the list Σ contains precisely the indices of the sites grid cells that touch the Minkowski sum of C_0 and $\lambda_{\max}P'$ (Figure 2-right).

In a multi-resolution sites grid, we use the pre-computed search-list only at the coarsest level of the sites grid. Then, when a cell should be recursively subdivided, we check that each sub-cell is at distance no more than the current minimal distance $\lambda \leq \lambda_{\max}$ found so far before examining the site(s) that it contains. Greene’s technique is easily modified to exit as soon as the cell is found to be farther from the query point than λ .

3.3 Computation of Σ with a spatially varying distance

When the parameters of the cone distance vary spatially, the distances to the sites grid cells must be conservatively under-approximated in order to account for the variation of the distances used at each different sites.

Both for computing the search list Σ and during the search of a nearest site for a given query point, we use a separate, larger distance cone P^{big} which is guaranteed to contain all the distance cones defined at the point sites $\{P(s) : s \in S\}$. Instead of computing λ_{\max} on this cone, we use the largest λ_{\max} among the values computed for all the possible distance cones: $\lambda_{\max}^{\text{big}} = \max_{s \in S} \lambda_{\max}(P(s))$. The search is then slower, but is sure to find the correct nearest site.

4 Elastic behavior and homogenization

For linear elasticity we have that $\sigma = C\epsilon$ and conversely $\epsilon = S\sigma$, where σ is the stress, ϵ is the strain, C is the elasticity tensor, and S is the compliance tensor.

We follow the conventional homogenization method [1] of prescribing the strain and computing the overall stress response for the six unit strains in order to approximate the elasticity tensor C . We obtain the compliance tensor S by directly inverting C .

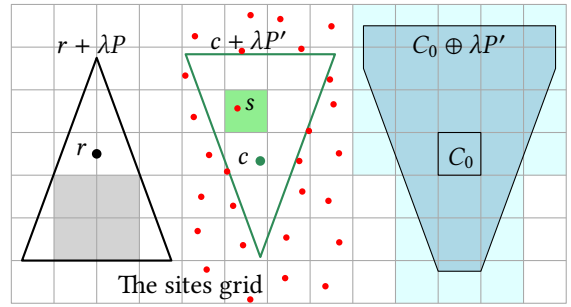


Figure 2: *Left.* One translate of the scaled polytope λP contains a 2×2 sub-grid. *Middle.* This guarantees that *any* translate of $\lambda P'$ contains at least one grid cell (green), thus at least one point site (red). *Right.* The blue cells have their index in the search list Σ .

4.1 Orthotropic materials

The compliance tensor S_{ortho} of an ideal orthotropic material [7] is:

$$S_{\text{ortho}} = \begin{pmatrix} s_{11} & s_{12} & s_{13} & 0 & 0 & 0 \\ s_{12} & s_{22} & s_{23} & 0 & 0 & 0 \\ s_{13} & s_{23} & s_{33} & 0 & 0 & 0 \\ 0 & 0 & 0 & s_{44} & 0 & 0 \\ 0 & 0 & 0 & 0 & s_{55} & 0 \\ 0 & 0 & 0 & 0 & 0 & s_{66} \end{pmatrix} \quad (12)$$

where,

$$s_{11} = \frac{1}{E_x}, \quad s_{22} = \frac{1}{E_y}, \quad s_{33} = \frac{1}{E_z} \quad (13)$$

$$s_{44} = \frac{1}{G_{yz}}, \quad s_{55} = \frac{1}{G_{zx}}, \quad s_{66} = \frac{1}{G_{xy}} \quad (14)$$

$$s_{12} = -\frac{\nu_{yx}}{E_y} = -\frac{\nu_{xy}}{E_x}, \quad s_{13} = -\frac{\nu_{zx}}{E_z} = -\frac{\nu_{xz}}{E_x}, \quad (15)$$

$$s_{23} = -\frac{\nu_{zy}}{E_z} = -\frac{\nu_{yz}}{E_y} \quad (16)$$

such that

$$\frac{\nu_{ij}}{E_i} = \frac{\nu_{ji}}{E_j} \quad i, j = x, y, z \quad i \neq j \quad (17)$$

and E_i is the Young’s modulus along axis i (measure of stiffness), G_{ij} , is the shear modulus in direction j on the plane whose normal is in direction i (measure of response to shear stress), and ν_{ij} is the Poisson’s ratio (ratio of transverse strain to axial strain) that corresponds to a contraction in direction j when an extension is applied in direction i .

Given an homogenized compliance tensor S , we compute the closest orthotropic compliance tensor S_{ortho} under the logarithmic Euclidean distance [8], which is well-suited for elasticity.

4.2 Bulk modulus

We are also interested in evaluating the overall compressive strength. To do so, we consider the bulk modulus K , that characterizes the tendency of a material to deform in all directions when uniformly loaded in all directions. A high bulk modulus implies higher material incompressibility. Given the following classical bulk modulus bounds [5]

6 Homogenized elasticity tensors Figure 16 in article

$$K_V = ((c_{11} + c_{22} + c_{33}) + 2(c_{12} + c_{23} + c_{31}))/9 \quad (\text{Voigt average})$$

$$K_R = ((s_{11} + s_{22} + s_{33}) + 2(s_{12} + s_{23} + s_{31}))^{-1} \quad (\text{Reuss average}) \quad (18)$$

we consider the Voigt-Reuss average $K_{VR} = (K_V + K_R)/2$.

5 Homogenized elasticity tensors Figure 15 in article

Tensors values are rounded to three decimals. Interestingly, the elasticity tensor of (Figure 15b) is well approximated by a monoclinic material (single plane of tensor symmetry, 13 independent constants), while the others are better approximated by an orthotropic one (three planes of tensor symmetry, 9 independent constants). For more details about tensor symmetries and elastic constants see for instance Section 2.2 in [7].

5.1 Figure 15a

$$C = \begin{pmatrix} 0.197 & 0.077 & 0.07 & 0.0 & 0.0 & 0.0 \\ 0.077 & 0.195 & 0.069 & 0.0 & 0.0 & 0.0 \\ 0.07 & 0.069 & 0.253 & 0.0 & 0.0 & 0.0 \\ 0.0 & 0.0 & 0.0 & 0.06 & 0.0 & 0.0 \\ 0.0 & 0.0 & 0.0 & 0.0 & 0.077 & 0.0 \\ 0.0 & 0.0 & 0.0 & 0.0 & 0.0 & 0.076 \end{pmatrix}$$

5.2 Figure 15b

$$C = \begin{pmatrix} 0.127 & 0.098 & 0.083 & 0.0 & -0.035 & 0.0 \\ 0.096 & 0.227 & 0.077 & 0.0 & -0.018 & 0.0 \\ 0.081 & 0.077 & 0.313 & 0.0 & -0.029 & 0.0 \\ 0.0 & 0.0 & 0.0 & 0.094 & 0.0 & -0.021 \\ -0.034 & -0.02 & -0.032 & 0.0 & 0.088 & 0.0 \\ 0.0 & 0.0 & 0.0 & -0.021 & 0.0 & 0.08 \end{pmatrix}$$

5.3 Figure 15c

$$C = \begin{pmatrix} 0.118 & 0.083 & 0.083 & 0.0 & 0.0 & 0.0 \\ 0.084 & 0.259 & 0.072 & 0.0 & 0.0 & 0.0 \\ 0.084 & 0.072 & 0.259 & 0.0 & 0.0 & 0.0 \\ 0.0 & 0.0 & 0.0 & 0.084 & 0.0 & 0.0 \\ 0.0 & 0.0 & 0.0 & 0.0 & 0.084 & 0.0 \\ 0.0 & 0.0 & 0.0 & 0.0 & 0.0 & 0.075 \end{pmatrix}$$

5.4 Figure 15d

$$C = \begin{pmatrix} 0.201 & 0.075 & 0.067 & 0.0 & 0.0 & 0.0 \\ 0.075 & 0.202 & 0.068 & 0.0 & 0.0 & 0.0 \\ 0.067 & 0.068 & 0.207 & 0.0 & 0.0 & 0.0 \\ 0.0 & 0.0 & 0.0 & 0.064 & 0.0 & 0.0 \\ 0.0 & 0.0 & 0.0 & 0.0 & 0.074 & 0.0 \\ 0.0 & 0.0 & 0.0 & 0.0 & 0.0 & 0.074 \end{pmatrix}$$

5.5 Figure 15e

$$C = \begin{pmatrix} 0.002 & 0.003 & 0.003 & 0.0 & 0.0 & 0.0 \\ 0.004 & 0.28 & 0.071 & 0.0 & 0.0 & 0.0 \\ 0.003 & 0.07 & 0.264 & 0.0 & 0.0 & 0.0 \\ 0.0 & 0.0 & 0.0 & 0.002 & 0.0 & 0.0 \\ 0.0 & 0.0 & 0.0 & 0.0 & 0.002 & 0.0 \\ 0.0 & 0.0 & 0.0 & 0.0 & 0.0 & 0.1 \end{pmatrix}$$

6.1 Left compression test ($\mu = 0.6, \sigma = 1$)

$$C = \begin{pmatrix} 0.06 & 0.024 & 0.019 & 0.0 & 0.0 & 0.0 \\ 0.024 & 0.061 & 0.019 & 0.0 & 0.0 & 0.0 \\ 0.018 & 0.019 & 0.058 & 0.0 & 0.0 & 0.0 \\ 0.0 & 0.0 & 0.0 & 0.017 & 0.0 & 0.0 \\ 0.0 & 0.0 & 0.0 & 0.0 & 0.026 & 0.0 \\ 0.0 & 0.0 & 0.0 & 0.0 & 0.0 & 0.026 \end{pmatrix}$$

6.2 Middle compression test ($\mu = 0.6, \sigma = 0.4$)

$$C = \begin{pmatrix} 0.012 & 0.016 & 0.012 & 0.0 & 0.0 & 0.0 \\ 0.018 & 0.16 & 0.042 & 0.0 & 0.0 & 0.0 \\ 0.013 & 0.042 & 0.145 & 0.0 & 0.0 & 0.0 \\ 0.0 & 0.0 & 0.0 & 0.012 & 0.0 & 0.0 \\ 0.0 & 0.0 & 0.0 & 0.0 & 0.017 & 0.0 \\ 0.0 & 0.0 & 0.0 & 0.0 & 0.0 & 0.059 \end{pmatrix}$$

6.3 Right compression test ($\mu = 0.85, \sigma = 1$)

$$C = \begin{pmatrix} 0.06 & 0.03 & 0.023 & 0.0 & 0.0 & 0.0 \\ 0.031 & 0.06 & 0.024 & 0.0 & 0.0 & 0.0 \\ 0.025 & 0.025 & 0.148 & 0.0 & 0.0 & 0.0 \\ 0.0 & 0.0 & 0.0 & 0.013 & 0.0 & 0.0 \\ 0.0 & 0.0 & 0.0 & 0.0 & 0.035 & 0.0 \\ 0.0 & 0.0 & 0.0 & 0.0 & 0.0 & 0.035 \end{pmatrix}$$

References

- [1] ANDREASSEN, E., AND ANDREASEN, C. S. How to determine composite material properties using numerical homogenization. *Computational Materials Science* 83 (2014), 488–495.
- [2] CHEN, Z., PAPADOPOULOU, E., AND XU, J. Robustness of k-gon Voronoi diagram construction. *Information Processing Letters* 97, 4 (2006), 138–145.
- [3] DEHNE, F., AND KLEIN, R. “The big sweep”: On the power of the wavefront approach to voronoi diagrams. *Algorithmica* 17, 1 (1997), 19–32.
- [4] GREENE, N. Detecting intersection of a rectangular solid and a convex polyhedron. In *Graphics Gems IV*, P. S. Heckbert, Ed. Academic Press, 1994, ch. I.7, pp. 74–82.
- [5] HILL, R. The elastic behaviour of a crystalline aggregate. *Proceedings of the Physical Society. Section A* 65, 5 (1952), 349.
- [6] ICKING, C., AND HA, L. A tight bound for the complexity of voronoi diagrams under polyhedral convex distance functions in 3D. In *Proceedings of the Thirty-third Annual ACM Symposium on Theory of Computing* (2001), pp. 316–321.
- [7] JONES, R. M. *Mechanics of Composite Materials*, vol. 193. Scripta Book Company Washington, DC, 1975.
- [8] MOAKHER, M., AND NORRIS, A. N. The closest elastic tensor of arbitrary symmetry to an elasticity tensor of lower symmetry. *Journal of Elasticity* 85, 3 (2006), 215–263.

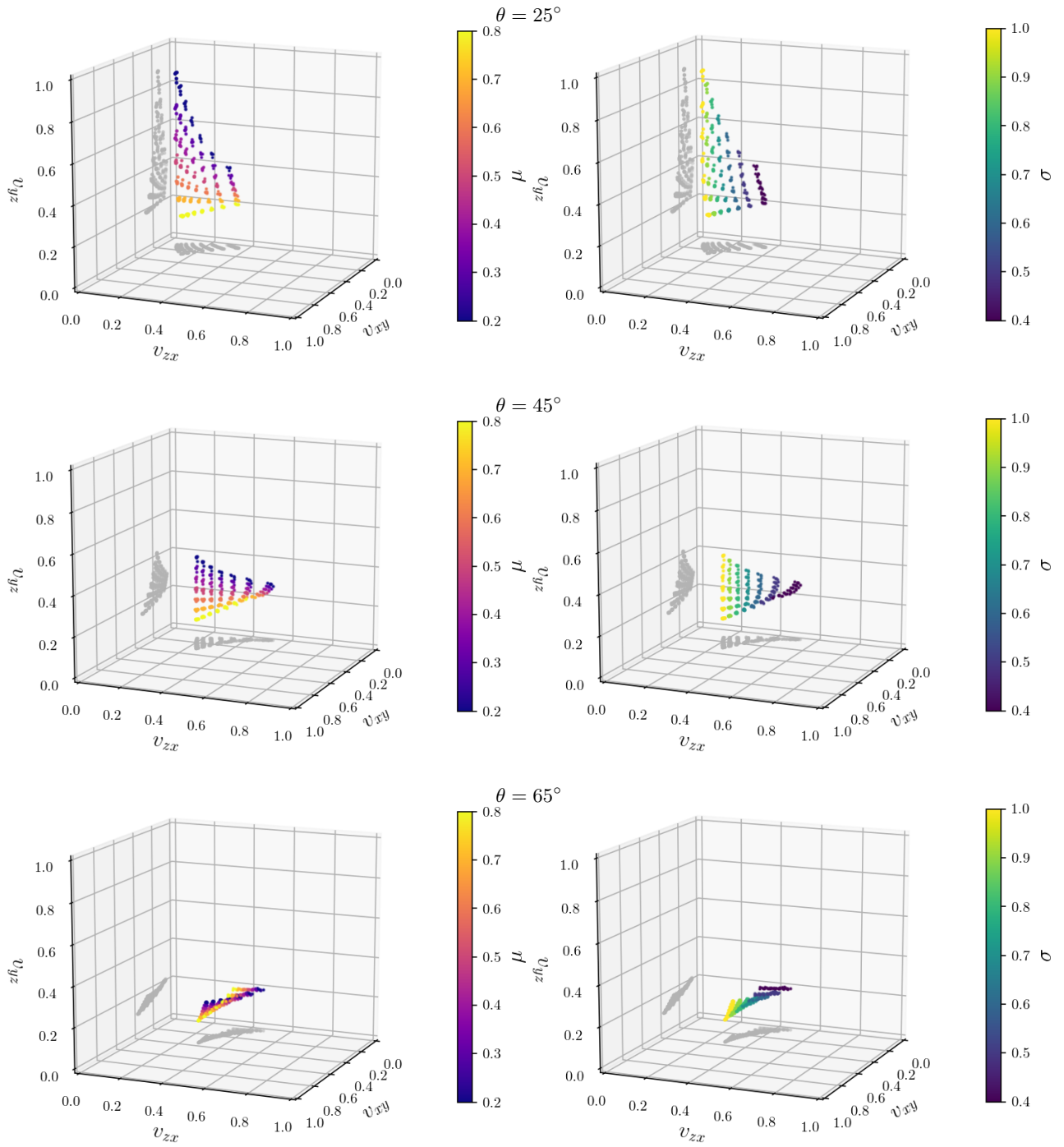


Figure 3: Material space for $k = 8$. Each row corresponds to a different minimal bisector slope θ . Each plot dot denotes a single test. The plot axes correspond the three orthogonal Poisson's ratio. The color of dots either depicts μ (left column) or σ (right column).

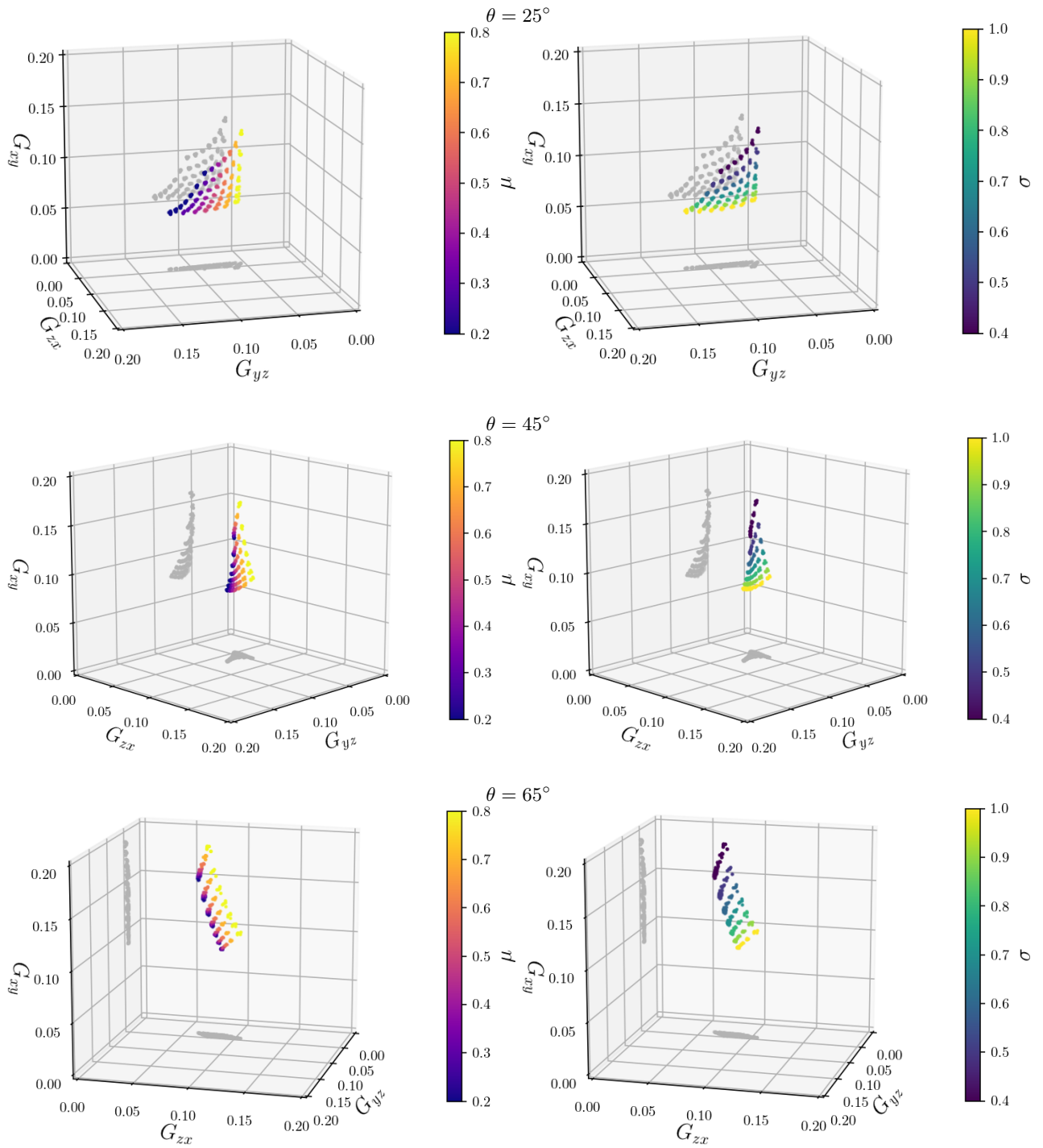


Figure 4: Material space for $k = 8$. Each row corresponds to a different minimal bisector slope θ . Each plot dot denotes a single test. The plot axes correspond the three orthogonal shear moduli. The color of dots either depicts μ (left column) or σ (right column).